RESEARCH ARTICLE SUMMARY

CARDIOLOGY

# Tracing the origins of de novo coronary collateral formation in cardiac repair

Mingjun Zhang†, Maoying Han†, Yangfeng Hou†, Zixin Liu†, Yilian Wang†, Xiuzhen Huang, Cheng Kiu Ho, Hang Qu, Qing-Dong Wang, Xin Ma, Kathy O. Lui*, Bin Zhou*

Full article and list of author affiliations: https://doi.org/10.1126/science.ady3027

**INTRODUCTION:** Coronary artery disease remains a leading cause of death worldwide. Acute occlusion of a coronary artery deprives downstream myocardium of oxygen and nutrients, precipitating myocardial infarction (MI). Coronary collateral arteries, which serve as natural bypass conduits between preexisting coronary artery branches, can restore perfusion to ischemic tissue and improve clinical outcomes. However, the cellular origin and molecular regulation of de novo collateral artery formation remain incompletely defined. Conventional lineage tracing has been constrained by imperfect marker specificity and the temporally variable nature of tamoxifen-dependent labeling.

**RATIONALE:** To delineate the cellular origin of coronary collaterals, we engineered complementary genetic lineage–tracing systems. These include intersectional strategies that reduce false-positive labeling and a cell-cell contact-triggered system that permanently marks mature arterial endothelial cells (ECs) without tamoxifen. We also developed tools to label capillary-derived and artery-derived vessels simultaneously within the same animal, enabling direct comparison of distinct EC sources after MI, and we interrogated the signaling pathways that govern this process.

**RESULTS:** We identified a subset of capillary ECs that express the arterial marker Cx40, highlighting specificity limitations of conventional tracing. Across multiple independent systems, including intersectional genetics and a synthetic Notch-based method, we found that mature arterial ECs contribute modestly to new collaterals after MI. Concurrent tracing within single hearts revealed that capillary ECs constitute the primary building blocks of collateral arteries in both neonatal and adult mice, with a modest contribution from preexisting arterial ECs. Selective ablation of capillary-derived collaterals impaired repair, increased fibrosis, and worsened cardiac function, establishing their functional necessity. To enhance collateralization, we modulated vascular endothelial growth factor (VEGF) signaling. Sustained pathway activation expanded immature arterial-like ECs but failed to improve repair. By contrast, transient delivery of *Vegfa* by using modified mRNA promoted functional collaterals, improved perfusion, reduced scarring, and enhanced cardiac function after injury. Mechanistically, VEGF-A activated the transcription factor YY1 (yin yang 1), which recruited the chromatin regulator SETD1A to promote histone H3 lysine 4 trimethylation (H3K4me3) and induce the arterial regulator *HES1* (hairy and enhancer of split–1), orchestrating capillary-to-artery conversion.

**CONCLUSION:** De novo coronary collaterals formed after MI arise primarily through arterialization of capillaries, with a modest contribution from preexisting arteries. We define a VEGF-A–YY1-SETD1A–HES1 epigenetic axis that orchestrates this process and demonstrate that transient VEGF stimulation can boost functional collateral formation and improve cardiac repair. These results position capillary arterialization as a central mechanism of endogenous revascularization and present a potential therapeutic strategy for ischemic heart disease. □

*Corresponding author. Email: kathyolui@cuhk.edu.hk (K.O.L.); zhoubin@sibs.ac.cn (B.Z.)
†These authors contributed equally to this work. **Cite this article as M. Zhang *et al.*, *Science* 393, eady3027 (2026). DOI: 10.1126/science.ady3027**

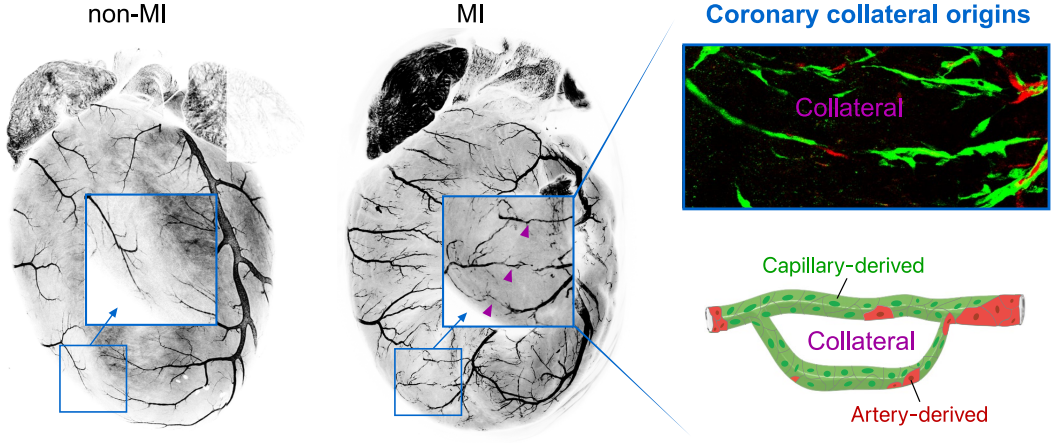


**Cellular origins of coronary collateral arteries.** Whole-mount imaging and schematic of neonatal mouse hearts under non-MI and MI (myocardial infarction) conditions. After injury, de novo coronary collaterals (purple arrowheads) form predominantly from capillary ECs (green) and modestly from preexisting arterial ECs (red).

CARDIOLOGY

# Tracing the origins of de novo coronary collateral formation in cardiac repair

Mingjun Zhang[1]†, Maoying Han[1]†, Yangfeng Hou[2]†, Zixin Liu[1]†, Yilian Wang[1]†, Xiuzhen Huang[1], Cheng Kiu Ho[2], Hang Qu[2], Qing-Dong Wang[3], Xin Ma[4], Kathy O. Lui[2]*, Bin Zhou[1,2,5,6]*

Coronary collateral arteries have been proposed to form de novo through artery reassembly, a process in which arterial endothelial cells (ECs) migrate away from preexisting arteries and reassemble into new arteries. Using genetic tools that trace arterial ECs, we found that their contribution to collaterals is modest. Dual genetic lineage tracing revealed that capillary ECs, rather than arterial ECs, serve as the major building blocks for de novo collaterals. The capillary-to-collateral conversion is functionally crucial for cardiac repair. In addition, transient *Vegfa* expression through modified messenger RNA markedly promoted collateral formation. Mechanistically, vascular endothelial growth factor (VEGF) drives arterialization by regulating HES1 transcription through YY1/SETD1A-mediated H3K4 trimethylation. Collectively, these findings redefine the cellular origin and mechanism of coronary collateral formation and highlight its role in facilitating efficient cardiac repair.

Coronary artery disease remains one of the leading causes of mortality and morbidity worldwide (*1*). Occlusion of coronary arteries obstructs blood flow to downstream cardiomyocytes, leading to myocardial infarction (MI). Conventional therapeutic strategies such as coronary stenting and coronary artery bypass grafting can restore blood supply to ischemic regions. However, these procedures are invasive and pose risks, including reperfusion injuries, highlighting the need for alternative approaches that enable a more gradual, endogenous restoration of blood flow to improve the recovery of damaged heart tissue (*2*). Coronary collaterals serve as natural bypasses in the heart, effectively supplying blood to ischemic myocardium, and are associated with improved outcomes in coronary artery disease (*3*–*5*). Therefore, there is an urgent need for strategies that promote collateral artery formation. Despite its clinical relevance, the cellular and molecular mechanisms underlying the generation of coronary collaterals remain incompletely understood.

Coronary collaterals typically form through arteriogenesis, in which preexisting arterial shunts enlarge in response to shear stress as a result of coronary obstruction (*2*, *6*, *7*). However, many patients lack sufficient preexisting arterial shunts for collateral development after injury (*5*). Recent studies revealed that collateral arteries can also form de novo, independently of preexisting shunts (*8*–*13*), offering an alternative pathway for collateral formation (*11*, *14*). In the prevailing model, arterial ECs migrate out, proliferate, and reassemble into collateral arteries (*12*, *15*). This "artery reassembly" model is supported by lineage-tracing studies that use the tamoxifen (Tam)–inducible *Cx40-CreER* tool. However, prolonged exposure or delayed degradation of Tam can result in extended labeling beyond the intended time frame (*16*). Because collaterals begin forming as early as 1 to 2 days after MI (*11*, *12*), residual Tam activity may label newly formed collaterals that acquire connexin 40 (Cx40) expression, potentially confounding lineage-tracing results. Moreover, the specificity of *Cx40-CreER* for arterial ECs is not exclusive because $Cx40^+$ capillary ECs can also contribute to collateral formation after MI (Fig. 1), further complicating the interpretation of *Cx40-CreER*–based lineage-tracing results. Furthermore, recent studies suggested that sprouting angiogenesis also contributes to coronary collateral in myocardial ischemia models (*13*, *17*). Therefore, the precise cellular origin of de novo collateral formation remains unresolved.

YY1 (yin yang 1) has emerged as an important regulator in diverse biological processes, including angiogenesis and vascular remodeling, and is among the most highly up-regulated transcriptional regulators in sprouting ECs (*18*–*20*). A recent study further demonstrated that YY1 regulates vascular resistance and blood pressure dynamics through epigenetic regulation of vascular smooth muscle cells (SMCs) (*21*). However, the role of YY1 in ECs during collateral artery development remains poorly understood. The Notch signaling pathway and its downstream effector HES1 (hairy and enhancer of split–1) are key regulators of arterial specification, EC proliferation, and angiogenesis (*22*, *23*). Despite the importance of these pathways, the mechanisms regulating HES1 during collateral formation remain unknown.

In this study, we applied a cell-cell contact-triggered genetic lineage–tracing system to specifically trace arterial ECs in a Tam-independent and arterial EC-marker-free manner. Furthermore, we developed a method to simultaneously label both capillary ECs and artery ECs with distinct fluorescent reporters within a single mouse. Using these genetic tools, we found that coronary collaterals in mouse hearts primarily originated from local capillary ECs through arterialization, rather than from arterial ECs through artery reassembly. The contribution of capillary ECs to collateral formation is functionally crucial for heart repair and regeneration and is promoted by treatment with *Vegfa*-modified mRNA. Mechanistically, vascular endothelial growth factor (VEGF) regulates HES1 transcription through YY1-mediated histone H3 lysine 4 trimethylation (H3K4me3) to drive arterialization. These findings offer insights into the mechanisms that drive de novo coronary collateral formation.

## Genetic labeling of $Cx40^+$ cells and their role in collateral formation

Previous research reported that Cx40 specifically labels arterial ECs but not capillary ECs in the neonatal heart (*12*). However, using the same *Cx40-CreER–RFP* mice (*12*, *24*, *25*), we found that a subset of $Cx40^+$ ECs marked by the red fluorescent protein (RFP) reporter of *Cx40-CreER-RFP* were not encircled by SMCs (Fig. 1A) but instead were scattered within the capillary network in the postnatal day 0 (P0) heart (Fig. 1B). These cells accounted for $0.34 \pm 0.09\%$ of total coronary ECs and $21.58 \pm 6.19\%$ of $Cx40^+$ ECs (Fig. 1C). Given that arterial ECs are surrounded by SMCs, a key distinction from capillary ECs (*14*, *26*), this observation suggests that Cx40 marks a subset of capillary ECs in addition to arterial ECs in the neonatal heart. To validate this observation, we performed single-cell RNA-sequencing (scRNA-seq) on coronary ECs isolated from P2 mouse hearts (fig. S1, A to D). By combining the capillary marker *Apln* with *Cx40* expression, we identified an $Apln^+Cx40^+$ EC population in which 75.84% was capillary ECs and 24.16% was preartery cells (Fig. 1D and fig. S1B). Pseudotime analysis

[1]CAS CEMCS-CUHK Joint Laboratory, New Cornerstone Science Laboratory, Key Laboratory of Multi-Cell Systems, Shanghai Institute of Biochemistry and Cell Biology, Center for Excellence in Molecular Cell Science, Chinese Academy of Sciences, University of Chinese Academy of Sciences, Shanghai, China. [2]CAS CEMCS-CUHK Joint Laboratory, Department of Chemical Pathology, Li Ka Shing Institute of Health Sciences, The Chinese University of Hong Kong, Prince of Wales Hospital, Hong Kong, China. [3]Bioscience Cardiovascular, Research and Early Development, Cardiovascular, Renal and Metabolism, BioPharmaceuticals R&D, AstraZeneca, Gothenburg, Mölndal, Sweden. [4]Department of Pharmacology, Wuxi School of Medicine, Jiangnan University, Wuxi, China. [5]Key Laboratory of Systems Health Science of Zhejiang Province, School of Life Science, Hangzhou Institute for Advanced Study, University of Chinese Academy of Sciences, Hangzhou, China. [6]School of Life Science and Technology, ShanghaiTech University, Shanghai, China. ***Corresponding author. Email: kathyolui@cuhk.edu.hk (K.O.L.); zhoubin@sibs.ac.cn (B.Z.)** †These authors contributed equally to this work.

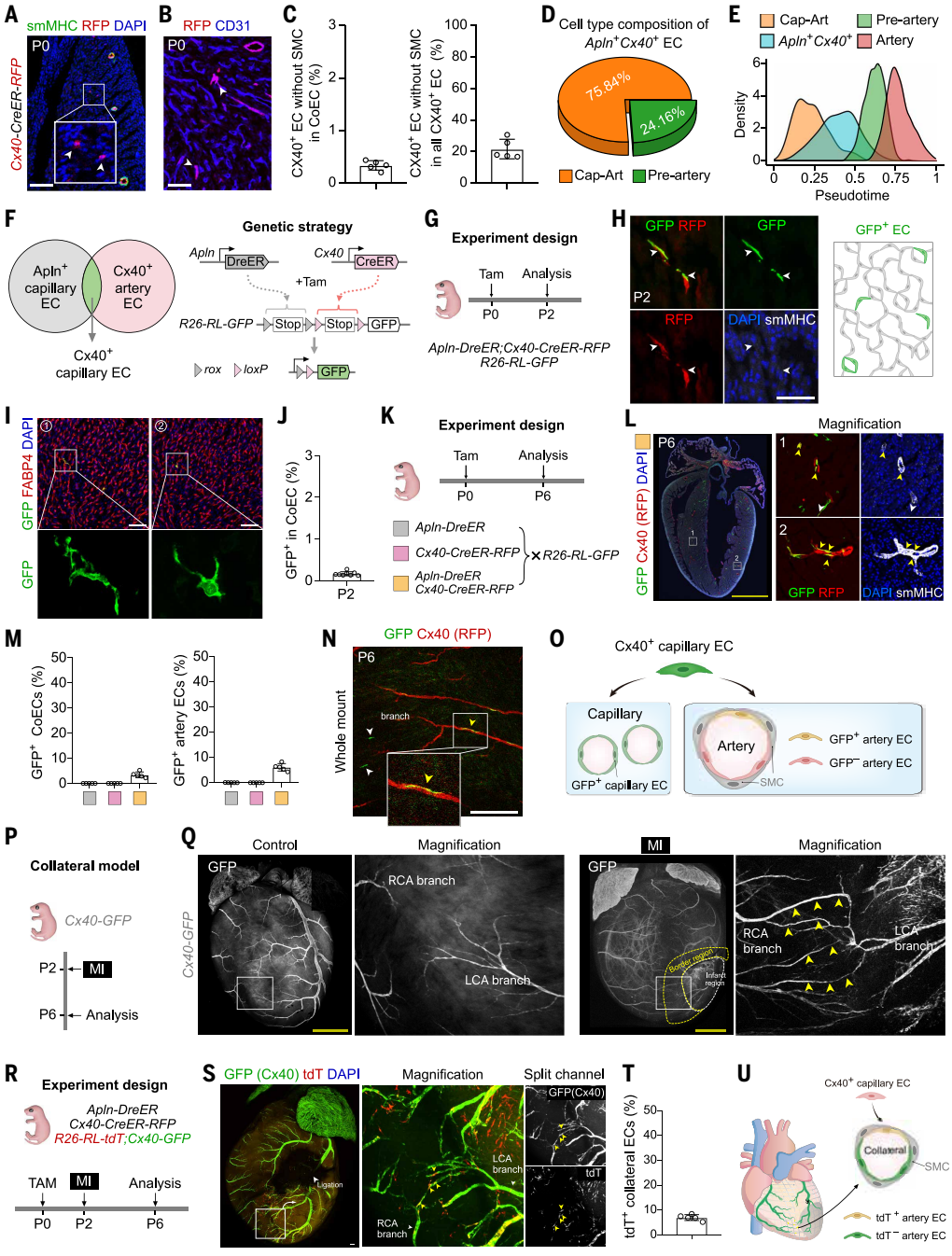


**Fig. 1. *Cx40-CreER* labels capillary ECs that contribute to collateral formation.** (**A**) Immunostaining for RFP and smooth muscle myosin heavy chain (smMHC) on heart sections of P0 *Cx40-CreER-RFP* mice. Arrowheads indicate Cx40$^+$ ECs that are not surrounded by SMCs. (**B**) Immunostaining for RFP and CD31 on heart sections of P0 *Cx40-CreER-RFP* mice. (**C**) Quantification of the percentage of Cx40$^+$ ECs lacking SMC coverage among (left) all coronary ECs (CoECs) and (right) all Cx40$^+$ ECs. Data are presented as mean ± SD; $n = 5$ mice. (**D**) Pie chart displaying the cell type composition of *Apln*$^+$*Cx40*$^+$ ECs. The population is predominantly composed of capillary ECs (Cap-Art, 75.84%, orange) and preartery cells (24.16%; green). (**E**) Pseudotime-ordered density plot depicting the relative abundance and distribution of various endothelial subpopulations during the differentiation process. (**F**) A schematic illustrating the strategy for tracing Cx40$^+$ capillary EC. A schematic showing the genetic lineage tracing strategy. (**G**) A schematic depicting the experimental design. (**H**) Immunostaining for GFP, RFP, and smMHC on heart sections of P2 *Apln-DreER;Cx40-CreER-RFP;R26-RL-GFP* mice. Arrowheads indicate GFP$^+$ ECs without SMCs. (**I**) Immunostaining for GFP and FABP4 on P2 serial heart sections. (**J**) Quantification of GFP$^+$ ECs among all CoEC. Data are presented as mean ± SD; $n = 8$ mice. (**K**) A schematic showing the experimental design. (**L**) Immunostaining for GFP, RFP, and smMHC on heart sections of P6 *Apln-DreER;Cx40-CreER-RFP;R26-RL-GFP* mice. Arrowheads indicate GFP$^+$ arterial ECs. (**M**) Quantification of the percentage of GFP$^+$ ECs in all (left) CoECs or (right) arteries. Data are presented as mean ± SD; $n = 5$ mice. (**N**) Whole-mount fluorescence confocal image of a P6 heart. White arrowheads indicate GFP$^+$ capillaries; yellow arrowheads indicate GFP$^+$ arteries. (**O**) A cartoon showing that Cx40$^+$ capillary ECs contribute to the capillary network and artery formation during neonatal heart growth. (**P**) A schematic showing the experimental design. (**Q**) Whole-mount fluorescence confocal image of P6 *Cx40-GFP* mice hearts after (left) non-MI control or (right) MI. Arrowheads indicate collaterals. (**R**) A schematic showing the experimental design. (**S**) Whole-mount fluorescence confocal image of P6 *Apln-DreER;Cx40-CreER-RFP;R26-RL-tdT;Cx40-GFP* mice after MI. Yellow arrowheads indicate tdT$^+$ collateral ECs. (**T**) Quantification of the percentage of tdT$^+$ ECs among collateral artery ECs. Data are presented as mean ± SD; $n = 5$ mice. (**U**) A cartoon showing that Cx40$^+$ capillaries contribute to collateral formation after MI. Scale bars, 1 mm (yellow); 100 μm (white).

revealed a differentiation trajectory from capillary ECs to preartery cells and subsequently to arterial ECs (Fig. 1E and fig. S1E), indicating the presence and artery-forming potential of $Cx40^+$ capillary ECs.

To trace the fate of these $Cx40^+$ capillary ECs during normal heart growth, we applied a dual recombinase lineage-tracing system (*27*), combining Cx40 and the capillary EC marker Apln (*14*, *28*) to drive two orthogonal recombinases (Fig. 1F). Specifically, the intersection of *Apln-DreER* (*29*), *Cx40-CreER-RFP* (*12*) with *R26-RL-GFP* reporter mouse (*30*) enables selective labeling of $Apln^+Cx40^+$ capillary ECs as green fluorescent protein–positive ($GFP^+$) after Tam treatment (Fig. 1F). Tam was administered at P0, and heart samples were collected at P2 to label $Cx40^+$ capillary ECs (Fig. 1G). Immunostaining revealed that $GFP^+$ ECs lacked SMC encirclement, and some exhibited morphological features similar to those of tip cells (Fig. 1, H and I). These $GFP^+$ ECs accounted for 0.18 ± 0.05% of total coronary ECs (Fig. 1J). By P6, whole-mount and immunostaining results showed that some $GFP^+$ ECs had integrated into arteries (Fig. 1, K to N, and fig. S1, F to H), which is consistent with the pseudotime trajectory analysis (fig. S1E). Quantitatively, these prelabeled $Cx40^+$ capillary ECs contributed to 3.40 ± 1.15% of capillary ECs ($FABP4^+$) and 6.13 ± 1.47% of arterial ECs (covered by SMCs) at P6 (Fig. 1M). To examine the leakiness potential of CreER (*31*) and Cre-*rox* or Dre-*loxP* recombination (*32*), we performed the following validation experiments: No $GFP^+$ ECs were detected in mice without Tam treatment (fig. S1I), and no $GFP^+$ ECs were observed in *Apln-DreER;R26-RL-GFP* or *Cx40-CreER-RFP;R26-RL-GFP* hearts treated with Tam (Fig. 1M and fig. S1J). Clonal analysis by using *Apln-DreER;Cx40-CreER;R26-Confetti2* mice revealed that the cell fate of individual $Cx40^+$ capillary ECs either incorporated into arteries or remained part of the capillary network, but not both (fig. S2, A to D). These results demonstrate that *Cx40-CreER* labels not only arterial ECs but also a subset of capillary ECs that incorporate into new arteries during postnatal heart growth (Fig. 1O).

In the mouse heart, collateral arteries form de novo as early as 1 to 2 days after MI (*11*, *12*). To investigate this, we induced MI in P2 mouse hearts and collected hearts for analysis at P6 (Fig. 1P, and fig. S2, E to H). In control hearts, we observed a watershed region that received blood from the distal branches of both the left coronary artery (LCA) and the right coronary artery (RCA) in P6 *Cx40-GFP* hearts (Fig. 1Q). After MI, collateral arteries formed de novo, spanning this watershed area and connecting the distal branches of the ligated LCA with the nonligated RCA (Fig. 1Q). Using *Apln-DreER;Cx40-CreER-RFP;R26-RL-GFP* mice, some $GFP^+$ ECs were integrated into a subset of arteries located in the border region where collateral formation occurs (fig. S2, I and J). To clearly visualize with whole-mount imaging this collateral's incorporation, we generated *Apln-DreER;Cx40-CreER;R26-RL-tdT;Cx40-GFP* mice, in which $Apln^+Cx40^+$ capillary ECs were labeled as tdT (tdTomato), and all arteries were visualized by means of *Cx40-GFP*. Mice were treated with Tam at P0 and subjected to MI at P2, and hearts were collected at P6 to examine the contribution of $tdT^+$ cells to $GFP^+$ collaterals (Fig. 1R). Whole-mount imaging and quantification showed that $tdT^+$ ECs accounted for 6.95 ± 1.17% of collateral ECs (Fig. 1, S and T), indicating that $Cx40^+$ capillary ECs contribute to collateral artery formation after MI (Fig. 1U). No leaky activation was detected in the absence of Tam after MI (fig. S2K).

We next used *Cx40-CreER-RFP;R26-tdT* to perform the same experiment by tracing $Cx40^+$ cells as previously described (*12*). We validated that the collateral arteries were largely $tdT^+$ (Fig. 2, A to C), recapitulating the experimental results from the previous study (*12*). However, these data highlight two important caveats of a *Cx40-CreER*–based genetic tracing system for arterial ECs. First, Cx40 is not restricted to arterial ECs but also labels a subset of capillary ECs. Second and possibly more critically, because Tam may not be completely washed out after MI, and newly formed collaterals also express Cx40 (Fig. 1Q), collateral ECs are possibly labeled by *Cx40-CreER* rather than originating from preexisting arterial ECs. In the time-sensitive studies that used Tam-dependent models, this limitation would inflate the apparent contribution of preexisting arterial ECs and lead to the potential false-positive interpretation that the labeled collaterals originate from preexisting arterial ECs.

## Coronary collaterals modestly develop through artery reassembly

To increase stringency and minimize the false-positive labeling from residual Tam, we first designed an intersectional genetic strategy that requires two independent recombination events for labeling (Fig. 2D). We combined an arterial EC-specific driver (*Bmx-CreER*) (*33*) and a *Cx40-DreER* driver (fig. S3) with a dual-recombinase reporter (*R26-RL-tdT*) so that tdT expression occurred only after both CreER-*loxP* and DreER-*rox* recombinations in the same cell (Fig. 2E). After Tam treatment at P0, 97.77 ± 0.79% of arterial ECs were $tdT^+$ at P2 (Fig. 2, F and G). For comparison, we used conventional *Cx40-CreER-RFP;R26-tdT* mice as controls (*12*). All mice were treated with Tam at P0, subjected to MI at P2, and analyzed at P6. Whole-heart confocal imaging showed that the number of $tdT^+$ arterial EC–derived collaterals were markedly reduced in the intersectional system compared with conventional *Cx40-CreER* controls (Fig. 2, H and I). Second, we designed another intersectional system by generating *Bmx-CreER;Cx40-LSL-Dre;R26-RL-tdT;Cx40-GFP* mice, in which tdT expression occurs only when two CreER-*loxP* and one Dre-*rox* recombination events have been induced (Fig. 2J). Two days after Tam treatment, 96.04 ± 0.92% of arterial ECs were $tdT^+$ (Fig. 2, K to M). After MI at P2 and analysis at P6 (Fig. 2N), whole-heart confocal imaging revealed that although preexisting arteries were largely $tdT^+GFP^+$, the percentage of $GFP^+$ ECs expressing tdT in collaterals was 23.02 ± 2.92% (Fig. 2, O to P).

Next, we developed a genetic approach to label and trace mature arterial ECs through their interaction with neighboring SMCs by using a synthetic Notch (synNotch) signaling pathway (*34*, *35*). In this system, Membrane-tethered GFP (mGFP) was expressed in SMCs as sender cells, whereas ECs expressed an artificial Notch receptor as receiver cells. For the artificial receptor, the extracellular and intracellular domains of the Notch protein were replaced with a Myc-tagged anti-GFP nanobody (αGFP) and the tetracycline transactivator (tTA), respectively, creating the construct αGFP-N-tTA (Fig. 3A). Upon contact between SMCs and ECs, the intracellular tTA domain in ECs was cleaved and translocated into the nucleus, where it activated the *tet*-responsive locus to initiate the expression of downstream genes, such as Dre recombinase. This process leads to Dre-mediated recombination of the *R26-rox-tdT* reporter (*36*), resulting in the permanent labeling of ECs by tdT (Fig. 3A). Because mature arterial ECs are typically surrounded by SMCs, whereas capillary ECs are not, this strategy selectively labels mature arterial ECs (Fig. 3A).

We first generated the *Myh11-mGFP* line, which specifically expressed GFP in SMCs (fig. S4, A to D) and effectively activated the synNotch system in ECs (fig. S4, E to H). To enable both transient and permanent labeling of mature arterial ECs that are covered by SMCs, we developed the *Myh11-mGFP;Cdh5-αGFP-N-tTA;tet-Dre-BFP;R26-rox-tdT* mouse model (Fig. 3A), in which blue fluorescent protein (BFP) marks ongoing EC-SMC contact, and tdT marks the history of such contact (Fig. 3A). Whole-mount fluorescence imaging and immunostaining of P2 hearts showed that mature arterial ECs were successfully traced as $tdT^+$, with them enveloped by $GFP^+$ SMCs (Fig. 3, B to D). Quantitative analysis revealed that 94.09 ± 2.99% of mature arterial ECs were $tdT^+$ (Fig. 3E), with even small-diameter arteries (<10 μm) exhibiting high tracing efficiency (Fig. 3F). No tdT labeling was detected in the absence of mGFP expression (fig. S4I). These results demonstrated the high efficiency and specificity of this intercellular genetic system in labeling mature arterial ECs through their SMC neighbors.

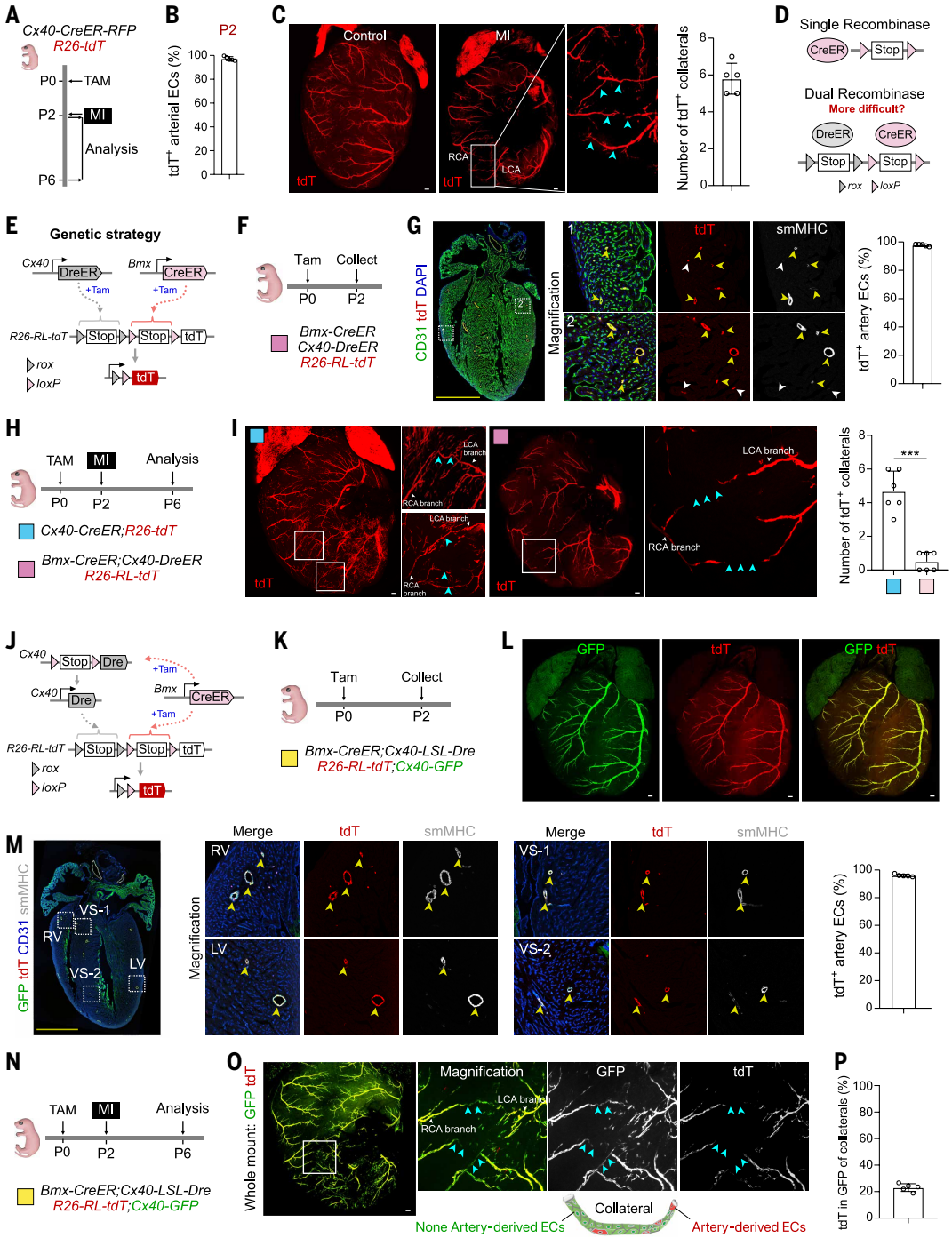


**Fig. 2. Assessment of arterial EC contribution to collaterals by intersectional genetic strategy.** (**A**) A schematic illustrating the experimental design. (**B**) Quantification of the percentage of arterial ECs expressing tdT from P2 *Cx40-CreER-RFP;R26-tdT* mice. Data are presented as mean ± SD; $n = 5$ mice. (**C**) Whole-mount fluorescence confocal image of P6 *Cx40-CreER-RFP;R26-tdT* mice after (left) non-MI control or (middle) MI. Arrowheads indicate collaterals. (Right) Quantification of the number of $tdT^+$ collaterals per heart. Data are presented as mean ± SD; $n = 5$ mice. (**D**) A schematic illustrating the hypothesis that residual Tam-mediated recombination is more difficult for dual recombinases than single recombinase. (**E**) A schematic illustrating the intersectional genetic strategy. (**F**) A schematic illustrating the experimental design. (**G**) Immunostaining for tdT, CD31, and smMHC on heart sections from P2 *Bmx-CreER;Cx40-DreER;R26-RL-tdT* mice. Yellow arrowheads indicate $tdT^+$ ECs with surrounding $smMHC^+$ cells; white arrowheads indicate $tdT^+$ ECs without surrounding $smMHC^+$ cells. (Right) Quantification of the percentage of arterial ECs expressing tdT. Data are presented as mean ± SD; $n =$ 5 mice. (**H**) A schematic illustrating the experimental design. (**I**) Whole-mount fluorescence confocal image of P6 MI heart from *Cx40-CreER-RFP;R26-tdT* mice or *Bmx-CreER;Cx40-DreER;R26-RL-tdT* mice. Cyan arrowheads indicated the collaterals. (Right) Quantification of $tdT^+$ collateral number per hearts from the indicated mice. Data are presented as mean ± SD; $n = 6$ mice; $^{***}P < 0.001$. (**J**) A schematic illustrating the second intersectional genetic strategy. (**K**) A schematic illustrating the experimental design. (**L**) Whole-mount fluorescence confocal image of P2 heart of *Bmx-CreER;Cx40-LSL-Dre;R26-RL-tdT;Cx40-GFP* mice. (**M**) Immunostaining for GFP, tdT, CD31, and smMHC on P2 heart sections. Yellow arrowheads indicate $tdT^+$ ECs with surrounding $smMHC^+$ cells. (Right) Quantification of the percentage of arterial ECs expressing tdT. Data are presented as mean ± SD; $n = 5$ mice. (**N**) A schematic illustrating the experimental design. (**O**) Whole-mount fluorescence confocal image of P6 MI heart. Arrowheads indicated the $GFP^+tdT^-$ collaterals. (**P**) Quantification of the percentage of collateral ECs expressing tdT. Data are presented as mean ± SD; $n = 5$ mice. Scale bars, 1 mm (yellow) and 100 μm (white).

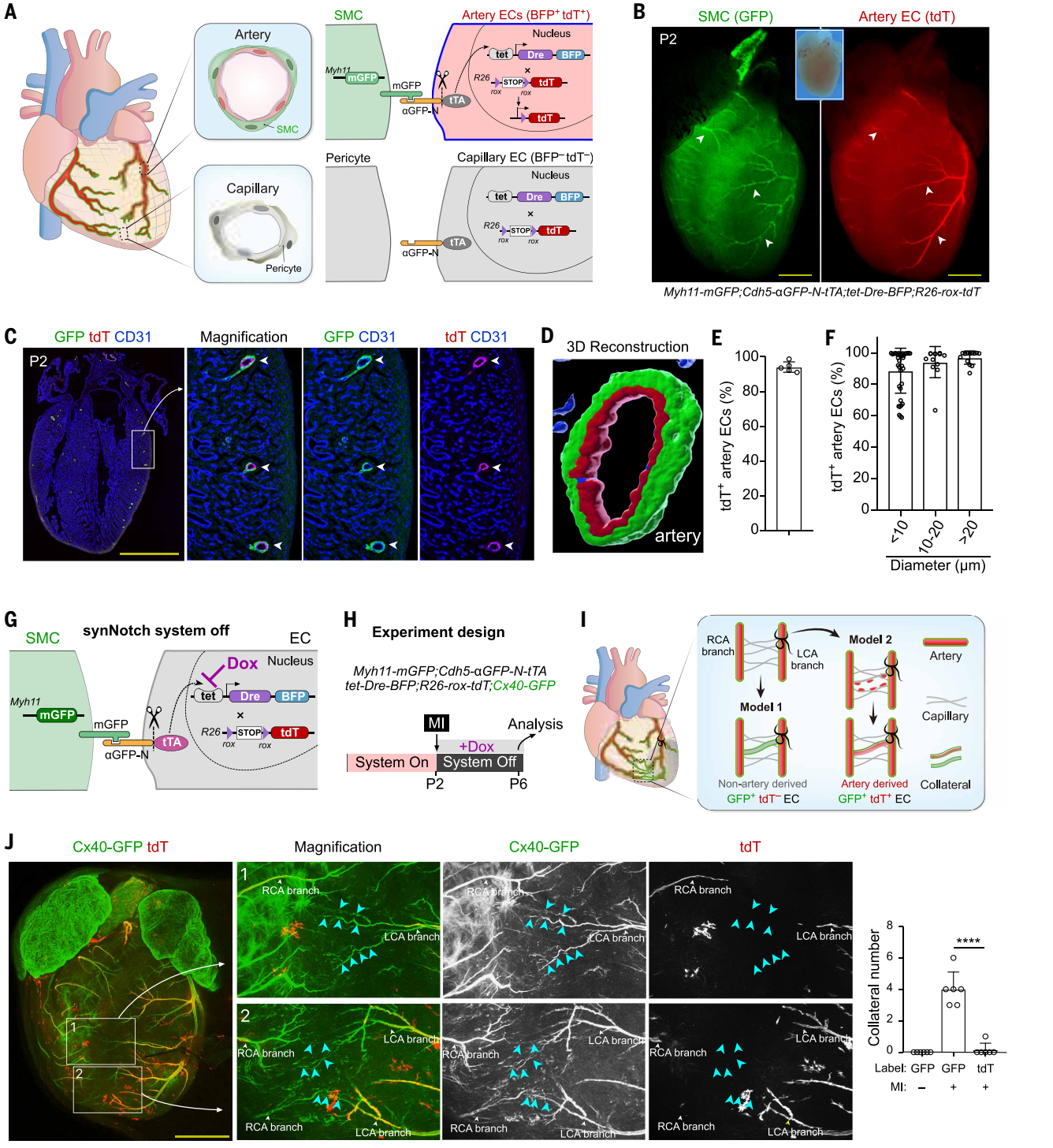


**Fig. 3. Arterial ECs modestly contribute to collateral formation after neonatal MI.** (**A**) A schematic illustrating the cell-cell contact-triggered genetic tracing of arterial ECs. (**B**) Whole-mount fluorescence images of P2 *Myh11-mGFP;Cdh5-αGFP-N-tTA;tet-Dre-BFP;R26-rox-tdT* mice hearts. Arrowheads indicate coronary arteries. (**C**) Immunostaining for GFP, tdT, and CD31 on heart sections of P2 *Myh11-mGFP;Cdh5-αGFP-N-tTA;tet-Dre-BFP;R26-rox-tdT* mice. Arrowheads indicate arteries. (**D**) A 3D reconstruction image of labeled arteries. (**E**) Quantification of the percentage of $tdT^+$ arterial ECs. Data are presented as mean ± SD; $n = 5$ mice. (**F**) Quantification of the percentage of $tdT^+$ arterial ECs by arterial diameters. Data are presented as mean ± SD; from five individual mice. (**G**) A schematic showing the Dox-induced inactivation of synNotch system. (**H**) A schematic illustrating the experimental design. (**I**) A cartoon depicting models of collateral formation. Model 1 represents collaterals derived from $GFP^+tdT^-$ nonarterial ECs, whereas model 2 represents collaterals derived from $GFP^+tdT^+$ arterial ECs. (**J**) Whole-mount fluorescence image showing GFP and tdT in P6 mouse hearts treated with Dox at P1 and subjected to MI at P2. Cyan arrowheads indicate coronary collaterals in the watershed area. (Right) Quantification of the number of collaterals per heart. Data are presented as mean ± SD; $n = 6$ mice. $^{****}P < 0.0001$. Scale bars, 1 mm (yellow).

The tTA-*tet* system used in our study can be effectively inhibited by doxycycline (Dox) (*35*). Consequently, all arterial ECs, including newly formed ones, are unable to activate Dre or BFP expression after Dox treatment, even when surrounded by GFP$^+$ SMCs (Fig. 3G). While the synNotch system is shut down by Dox, preexisting mature arterial ECs that were already labeled with tdT before Dox treatment continue to express tdT (Fig. 3G). We then created a genetic model by crossing *Myh11-mGFP;Cdh5-αGFP-N-tTA;R26-tetO-Dre-BFP;R26-R-tdT* mice with a *Cx40-GFP* reporter mouse.

Having optimized the tracing system, we induced MI at P2 and treated mice with Dox thereafter (Fig. 3H). Because the synNotch system is turned off after P2, preexisting arteries had already been permanently labeled as tdT$^+$ before MI. If coronary collaterals were derived from nonarterial ECs (model 1), the collaterals formed de novo would be GFP$^+$tdT$^-$. Conversely, if they were derived from preexisting arterial ECs through migration, proliferation, and reassembly as previously proposed (*12*), the coronary collaterals formed de novo would be GFP$^+$tdT$^+$ (Fig. 3I). Whole-mount fluorescence imaging revealed that the majority of coronary collaterals in the watershed region were composed of GFP$^+$tdT$^-$ ECs, with modest incorporation of GFP$^+$tdT$^+$ ECs (Fig. 3J). These results indicate that collateral arteries formed de novo are primarily derived from nonarterial ECs (model 1).

To confirm that synNotch-labeled ECs retain tdT expression after migrating away from SMCs and that the synNotch system does not interfere with EC migration, we examined intestinal vascular development, in which ECs move inward during villus formation (*37*) (fig. S4J). At embryonic day 13.5 (E13.5), the intestines exhibited an outer smooth muscle layer expressing the ligand mGFP, and vascular ECs connected to this layer were traced as tdT$^+$ (fig. S4K). After Dox treatment beginning at E13.5, tdT$^+$ ECs remained labeled while migrating away from SMCs to villus at E15.5 and E17.5 (fig. S4, L and M). In the absence of mGFP expression from SMCs, ECs showed no tdT leakiness (fig. S4N). These results demonstrate that the synNotch system effectively traces ECs that had prior contact with SMCs, even after their migration away from these cells (fig. S4O). In addition, scRNA-seq, vascular density, permeability, and perfusion analyses showed no obvious differences between synNotch mice and wild-type controls (fig. S5, A to I), indicating that the tracing system does not measurably alter EC behavior (fig. S5, A to I). We also observed proliferation of arterial ECs within the vessel lumen during neonatal heart growth (fig. S6), which contrasts with the rare arterial EC proliferation observed in adults during homeostasis (*38*, *39*).

## Capillary ECs are the primary source for collaterals in the injured heart

To simultaneously evaluate the contributions of arterial and capillary ECs to new artery formation within a single mouse, we aimed to develop a genetic system that enables distinct in vivo tracing of different EC populations. By crossing *Kdr-CreER* (fig. S7A) with the *R26-tdT* reporter line (*40*), we found efficient labeling of capillary ECs (98.48 ± 1.13%) with minimal labeling of arterial ECs (3.16 ± 0.91%) (fig. S7, B to F). This indicates that *Kdr-CreER* preferentially targets capillary ECs over arterial ECs. To specifically evaluate the contribution of arterial ECs, we developed an interleaved reporter line driven by the Cx40 promoter, called *Cx40-IR*. This model includes a *loxP-rox-Stop-loxP-GFP-pA-rox-tdT* cassette driven by the *Cx40* gene (fig. S7G). By crossing *Cx40-IR* with either *Actb-Cre* (*27*) or *Cx40-Dre* (*29*), we validated the successful generation of the *Cx40-IR* line, enabling arterial EC detection after either Cre-*loxP* or Dre-*rox* recombination (fig. S7, H to L).

We then generated *Kdr-CreER;Cx40-Dre;Cx40-IR* triple-positive mice (Fig. 4A). In this genetic system, preexisting Cx40$^+$ arterial ECs first activate *Cx40-Dre*, which labels the arteries as tdT$^+$ through Dre-*rox* recombination (Fig. 4A). Subsequent treatment with Tam activates *Kdr-CreER*, inducing Cre-*loxP* recombination of *Cx40-IR* allele. This results in the formation of a *Cx40-GFP* allele specifically in capillary ECs but not in arterial ECs (Fig. 4A). If these capillary ECs contribute to new artery formation, the *Cx40-GFP* reporter will then be activated, making the contribution readily detectable with whole-mount fluorescence imaging (Fig. 4A). We first analyzed the occupancy efficiency of *Cx40-Dre* at P2 (Fig. 4B). Immunostaining revealed that 98.14 ± 0.33% of arterial ECs were successfully traced as tdT$^+$, with minimal tdT expression observed in capillary ECs (Fig. 4, C and D). No GFP$^+$ ECs were detected in oil-treated *Kdr-CreER;Cx40-Dre;Cx40-IR* mice (fig. S7, M and N).

We next implemented an MI model to investigate the origins of coronary collaterals during heart repair. *Kdr-CreER;Cx40-Dre;Cx40-IR* mice were treated with Tam at P0, induced MI at P2, and were subsequently examined for coronary collateral formation in the watershed area at P6 (Fig. 4E). If the collateral arteries originated from capillary ECs, we would expect the newly formed collateral arteries to be predominantly GFP$^+$. Conversely, if they arose from the reassembly of arterial ECs, the majority would be tdT$^+$ (Fig. 4F). Whole-mount fluorescence imaging revealed that the collateral arteries spanning the watershed area were primarily GFP$^+$, with only a modest presence of tdT$^+$ ECs incorporated into the collaterals (Fig. 4G). By contrast, the main branches of the LCA and RCA remained predominantly tdT$^+$ (Fig. 4G). Quantification of collateral numbers showed that all collateral arteries contained GFP$^+$ ECs (Fig. 4H), with 85.71 ± 3.91% of collateral ECs being GFP$^+$ (Fig. 4I). To further validate this result, we independently used another capillary EC marker, Apln, to generate *Apln-CreER;Cx40-Dre;Cx40-IR* mice. This secondary strategy allowed for simultaneous and distinct tracing of capillary and arterial ECs. Using this approach, we found that Apln$^+$ capillary ECs represented the majority of ECs contributing to coronary collaterals (fig. S8, A to D). Collectively, these data confirm that capillary ECs are the major building blocks for the formation of coronary collaterals in the injured heart (Fig. 4J).

To investigate the reparative function of capillary-derived collaterals after neonatal MI, we developed a genetic ablation system specifically targeting capillary-derived arterial ECs (Fig. 4K). We generated *Cx40-IR-DTR* mice, in which a *loxP-rox-stop-loxP-GFP-DTR-pA-rox-tdT* construct was inserted into the *Cx40* gene. Subsequently, we created *Kdr-CreER;Cx40-Dre;Cx40-IR-DTR* mice, in which capillary-derived collateral ECs simultaneously express GFP and the diphtheria toxin receptor (DTR), whereas preexisting arterial ECs express tdT (Fig. 4K). Upon administration of diphtheria toxin (DT), DTR$^+$ collateral ECs would be genetically ablated (Fig. 4K). Tam was administered at P0, MI was induced at P2, and mice were subsequently treated with DT or phosphate-buffered saline (PBS); analysis was performed at P6 (Fig. 4L). Whole-mount imaging revealed abundant collateral arteries in PBS-treated hearts but no detectable collaterals after DT treatment (Fig. 4M). Sirius Red staining and immunostaining further showed increased fibrosis and larger cardiomyocyte defect areas in DT-treated hearts (Fig. 4, N and O). These results demonstrate that capillary-derived arteries are functionally essential for heart repair and regeneration in neonatal mice after MI.

We also investigated the process of new artery formation in a heart regeneration model by performing heart apex resection (AR) (*41*). *Kdr-CreER;Cx40-Dre;Cx40-IR* mice received Tam at P1, underwent AR at P4, and were analyzed 7 days later, a time point when new arteries were expected to form in the regenerated apex (fig. S8, E and F). Whole-mount confocal imaging of the regenerated apex revealed an abundance of GFP$^+$ arterial ECs, with relatively fewer tdT$^+$ arterial ECs (fig. S8, G and H). Immunostaining on heart sections further demonstrated that the newly formed arteries were primarily GFP$^+$, with only a small fraction of tdT$^+$ ECs incorporated into the arteries in the regenerated apex (fig. S8I). These results indicate that the ECs of the newly formed arteries in the regenerated apex were mainly derived from capillaries, with a modest fraction arising from the preexisting arteries after AR (fig. S8J).

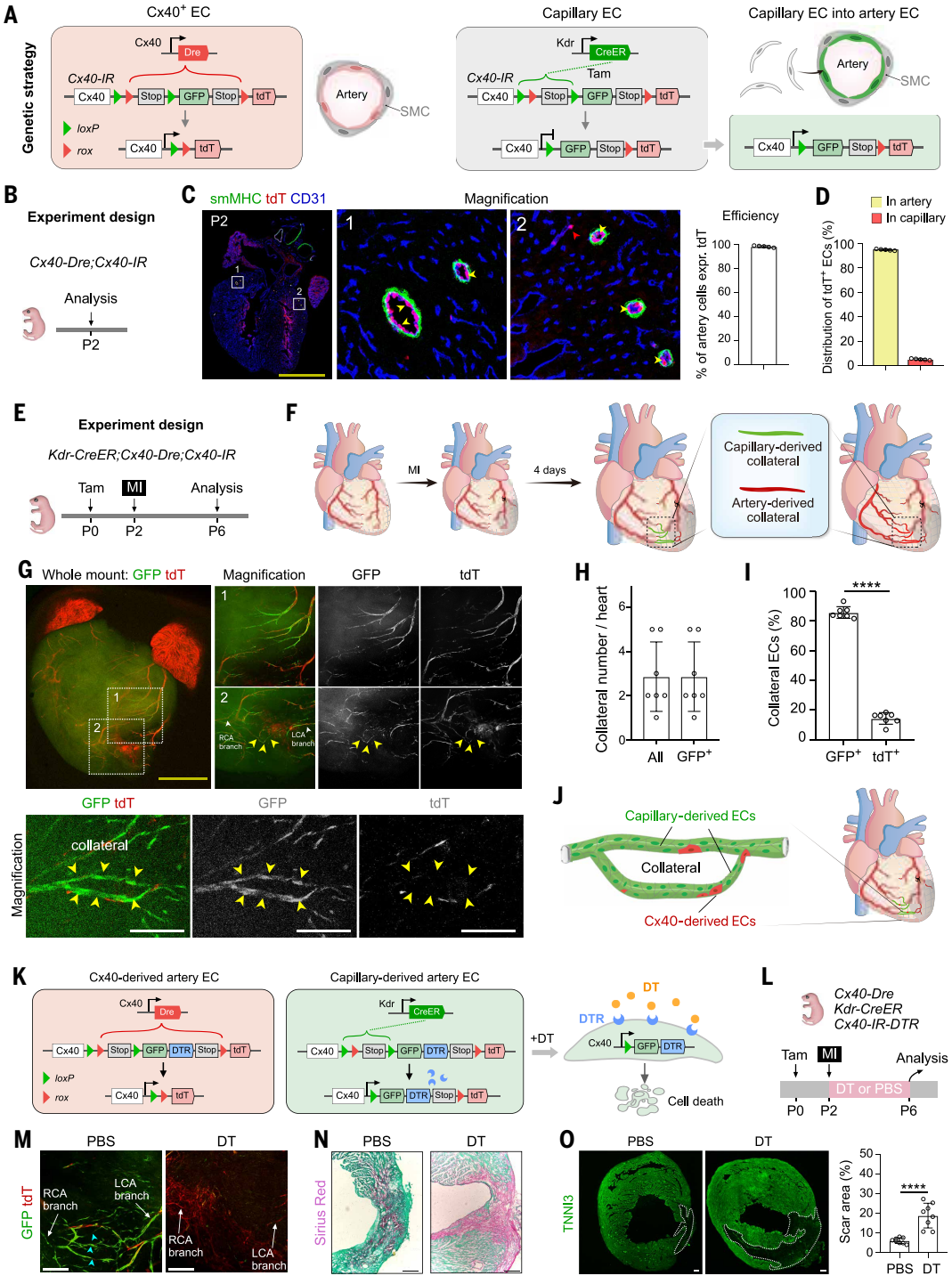


**Fig. 4. Capillary ECs contribute to new artery formation in neonatal mice.** (**A**) A cartoon illustrating the genetic tracing strategy. (**B**) A schematic showing the experimental design. (**C**) Immunostaining for smMHC, tdT, and CD31 on heart sections of P2 *Cx40-Dre;Cx40-IR* mice. (Right) Quantification of the percentage of artery ECs expressing tdT. Data are presented as mean ± SD; $n = 5$ mice. (**D**) Quantification of the percentage of arterial and capillary ECs consisting of $tdT^+$ ECs. Data are presented as mean ± SD; $n = 5$ mice. (**E**) A schematic illustrating the experimental design. (**F**) A cartoon depicting models of collateral artery formation. (**G**) Whole-mount fluorescence image of a P6 mouse heart after MI. Yellow arrowheads indicate $GFP^+$ collaterals in the watershed area. (**H**) Quantification of the number of collaterals per heart. Data are presented as mean ± SD; $n = 7$ mice. (**I**) Quantification of the percentage of arterial ECs expressing GFP or tdT. Data are presented as mean ± SD; $n = 7$ mice; $^{****}P < 0.0001$. (**J**) A cartoon showing that coronary collaterals are primarily derived from $GFP^+$ capillary ECs. (**K**) A cartoon illustrating the genetic tracing strategy for the genetic ablation of capillary-derived arteries. (**L**) A schematic showing the experimental design. (**M**) Whole-mount fluorescence image of a P6 MI heart treated with (left) PBS or (right) DT. (**N**) Sirius Red staining of heart sections of P6 MI hearts treated with (left) PBS or (right) DT. (**O**) Immunostaining for TNNI3 on heart sections of P6 MI heart treated with (left) PBS or (right) DT. Quantification of the percentage of scar area relative to the ventricular area is shown. Data are presented as mean ± SD; $n = 8$ mice; $^{****}P < 0.0001$. Scale bars, 1 mm (yellow); 100 μm (white or black).

## Capillary-derived collateral formation in adults after MI

To investigate the arterial formation capacity of capillaries in adults, *Kdr-CreER;Cx40-Dre;Cx40-IR* mice received Tam at 10 weeks, underwent MI at 12 weeks, and were analyzed 2 weeks later (Fig. 5A). In this experimental design, only capillary-derived new arteries could be traced as $GFP^+$, whereas capillaries themselves were not traceable unless their fate converted to arterial ECs (Fig. 4A). Whole-mount fluorescence imaging showed no $GFP^+$ capillary-derived arteries in control hearts (Fig. 5B). By contrast, a subset of $GFP^+$ capillary-derived arteries emerged in the watershed areas connecting $tdT^+$ arteries in MI hearts (Fig. 5C). Immunostaining further revealed that these $GFP^+$ arterial ECs were encircled by SMCs in the border and infarct regions of MI hearts (Fig. 5D). These findings indicate that capillaries contribute to the de novo formation of coronary collaterals, potentially supplying blood to the ischemic myocardium after MI.

Independently, we used another capillary EC marker, Apln, to lineage trace capillary ECs in adult hearts. Although Apln is robustly expressed in capillary ECs during embryonic and neonatal development (*14*, *42*, *43*), its expression is not maintained in most capillary ECs in the adult heart under homeostatic conditions but is reactivated after ischemic injury (*28*). To avoid the potential toxicity of continuous Tam treatment during the 2 weeks after MI, we opted not to use *Apln-CreER* for lineage tracing. Instead, we developed a genetic system to induce the generation of an *Apln-Dre* allele, enabling seamless recording of Apln-expressing cells through Dre-*rox* recombination at any time during the 2 weeks after MI (fig. S9A). In this approach, we used *Cdh5-CreER* (*44*) and a nested double reporter line (*R26-NR*) (*27*) to first trace all ECs by means of ZsGreen while simultaneously converting *Apln-LSL-Dre* into *Apln-Dre*. This setup primed the system to label $Apln^+$ capillary ECs whenever *Apln* was activated (fig. S9A). We treated mice with Tam at 10 weeks, performed MI at 12 weeks, and analyzed hearts 2 weeks later (fig. S9B). Immunostaining on heart sections indicated no $tdT^+$ arterial ECs in control hearts (fig. S9C). By contrast, a subset of arterial ECs in the border and infarct regions was $tdT^+$, whereas very few $tdT^+$ arterial ECs were observed in remote regions of MI hearts (fig. S9, D and E). These data demonstrate that capillary ECs contribute to the formation of newly generated arteries surrounding the infarcted myocardium, indicating the involvement of capillary-derived collaterals in the adult heart after injury.

VEGF signaling is essential for coronary angiogenesis and arterialization (*45*–*48*). To investigate whether VEGF-promoted angiogenesis facilitates the formation of capillary-derived collaterals in injured hearts, we overexpressed the VEGF receptor KDR (kinase insert domain receptor) in capillary ECs using the *Kdr-CreER;Cx40-Dre;Cx40-IR;H11-LSL-Kdr* model (Fig. 5E). Whole-mount fluorescence imaging and immunostaining revealed a marked increase in $GFP^+$ vessels in hearts overexpressing KDR compared with that in *Kdr-CreER;Cx40-Dre;Cx40-IR* controls (Fig. 5, F and G). The percentage of $GFP^+$ ECs among all $Cx40^+$ ECs increased from 14.58 ± 6.81% to 42.3 ± 15.72% after KDR overexpression in the border and infarct regions of MI hearts (Fig. 5H). In control hearts, $GFP^+$ ECs were predominantly encircled by SMCs, indicating their integration into mature arteries. However, in hearts overexpressing KDR, a considerable proportion of $GFP^+$ ECs were not surrounded by SMCs (Fig. 5G), suggesting incomplete arterial maturation after consistent VEGF overactivation. Further analysis showed no considerably reduced fibrosis (Fig. 5I) or improved cardiac function (Fig. 5J) in the hearts with KDR overexpression. These findings suggest that although VEGF signaling promotes the conversion of capillaries into $Cx40^+$ ECs, prolonged activation of VEGF signaling may impair the progression of these $Cx40^+$ ECs into fully mature arteries, resulting in limited improvement in cardiac function after MI.

To optimize therapeutic strategies for enhancing arterialization and improving cardiac function, we investigated whether increasing the local concentration of VEGF-A through *Vegfa* modified mRNA (modRNA), designed to transiently yet efficiently induce VEGF-A expression (*49*, *50*), could promote angiogenesis and arterialization in the injured myocardium. We induced MI and performed intramyocardial injection of modRNA in *Kdr-CreER;Cx40-Dre;Cx40-IR* mice at 12 weeks, after Tam treatment at 10 weeks (Fig. 5K). After intramyocardial injection of control luciferase (Luc) modRNA, bioluminescent imaging at 48 hours showed a robust Luc signal in the cardiac region (Fig. 5L), confirming successful cardiac delivery. Whole-mount fluorescence imaging and immunostaining revealed a marked increase in $GFP^+$ vessels in hearts treated with *Vegfa* modRNA compared with *Luc* modRNA controls (Fig. 5, M to O). Echocardiographic analysis further demonstrated an improvement in cardiac function after *Vegfa* modRNA treatment (Fig. 5P). Additionally, both immunostaining and Sirius Red staining indicated a notable reduction in scar regions treated with *Vegfa* modRNA compared with that of controls (Fig. 5, Q to S). Moreover, to assess functional integration of newly formed arteries, we performed lectin perfusion and Microfil-based micro–computed tomography (micro-CT). These $GFP^+$ arteries were perfused with lectin in both KDR-overexpressing and *Vegfa* modRNA–treated mice, indicating connectivity to the circulation (fig. S9, F and G). Micro-CT further showed a modest increase in coronary perfusion with KDR overexpression and a marked increase after *Vegfa* modRNA treatment (fig. S9, H to L). Combined *Vegfa* modRNA administration and KDR overexpression did not further improve cardiac function or myocardial protection compared with KDR overexpression alone, despite increasing $GFP^+$ capillary-derived immature arteries (fig. S9, M to P). These results suggest that transient overexpression of *Vegfa* through modRNA promotes the formation of capillary-derived functional arteries in adults after MI, enhancing cardiac repair and function after injury.

## VEGF-A regulates HES1 transcription through YY1-mediated H3K4me3

YY1 is one of the most strongly up-regulated transcriptional regulators in ECs during angiogenesis (*18*). In our study, *Yy1* was up-regulated in ECs after MI, following a dynamic pattern similar to that of *Vegfr2* (fig. S10, A to C). However, whether YY1 is regulated by VEGF-A and whether it functions in coronary collateral development remains unknown. To investigate this, we first asked whether VEGF-A regulates YY1 expression in ECs. Human embryonic stem cell–derived endothelial cells (hESC-ECs) were treated with VEGF-A for 48 hours. Western blot analysis showed a dose-dependent increase in endothelial YY1 expression (Fig. 6A), indicating that VEGF-A up-regulated YY1 in ECs. To investigate the role of YY1 in vivo, we generated a Yy1 floxed allele ($Yy1^{fl}$) and demonstrated that YY1 was functionally required for angiogenesis (fig. S10, D to N). To specifically examine whether YY1 regulates collateral formation after MI, we first confirmed that *Kdr-CreER* driver efficiently depletes *Yy1* in cardiac ECs (fig. S11, A to D). We then generated *Kdr-CreER;Cx40-Dre;Cx40-IR;*$Yy1^{fl/fl}$ mice to delete *Yy1* in capillary ECs while simultaneously tracking their contribution to collaterals (Fig. 6, B and C). Compared with control mice (*Kdr-CreER;Cx40-Dre;Cx40-IR*), mice in which *Yy1* was deleted exhibited a reduced contribution of capillary ECs to collaterals after MI (Fig. 6, D to F), accompanied by impaired cardiac function and increased scar formation (Fig. 6, G to I). To test whether YY1 mediates the procollateral effects of VEGF-A, we deleted *Yy1* in mice treated with *Vegfa* modRNA using the same *Kdr-CreER;Cx40-Dre;Cx40-IR;*$Yy1^{fl/fl}$ model (fig. S11E). Yy1 deletion markedly diminished the ability of *Vegfa* modRNA to promote capillary-to-collateral conversion (fig. S11F) and abolished the beneficial effects of *Vegfa* modRNA on cardiac function and fibrosis (fig. S11, G to K). These findings demonstrate that endothelial YY1 promotes collateral formation after MI and functions downstream of VEGF-A.

To determine the transcriptional program of YY1 in collateral artery development after injury, we isolated $CD31^+$ ECs from the hearts of non-MI control mice, MI wild type (MI-WT) mice, and mice in which

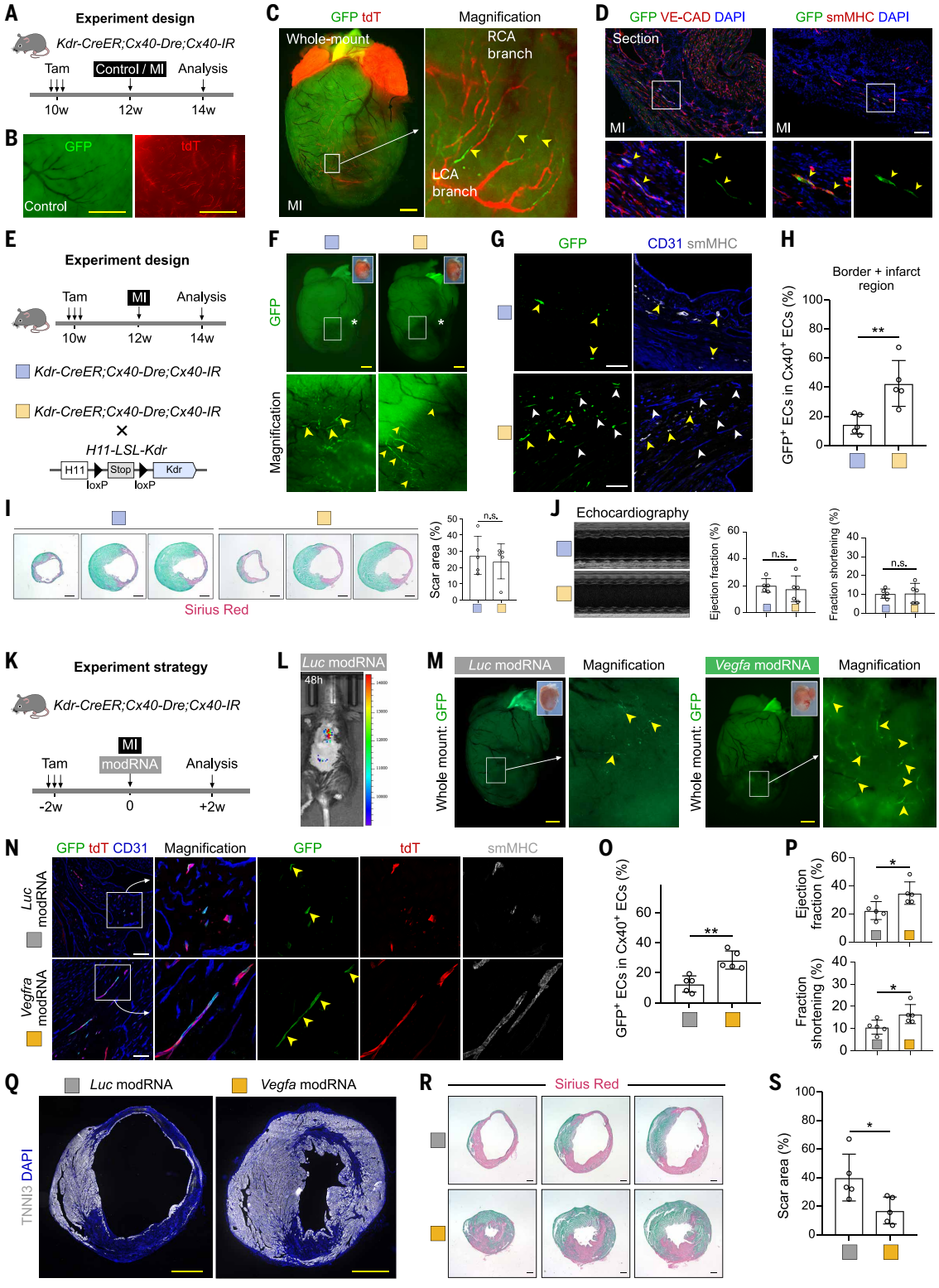


**Fig. 5. Promoting capillary-derived collaterals improves cardiac function in adult MI hearts.** (**A**) A schematic illustrating the experimental design. (**B**) Whole-mount fluorescence images of *Kdr-CreER;Cx40-Dre;Cx40-IR* hearts from non-MI control mice. (**C**) Whole-mount fluorescence images of *Kdr-CreER;Cx40-Dre;Cx40-IR* hearts after MI. Yellow arrowheads indicate GFP$^+$ collaterals in the watershed area of the adult MI heart. (**D**) Immunostaining for GFP, VE-CAD, and smMHC on MI heart sections. Arrowheads indicate GFP$^+$ collaterals in the border and infarct regions. (**E**) A schematic showing the experimental design. (**F**) Whole-mount fluorescence images of control and KDR-overexpression hearts. Arrowheads indicate GFP$^+$ vessels. (**G**) Immunostaining for GFP, CD31, and smMHC on heart sections. Yellow arrowheads indicate GFP$^+$ ECs surrounded by smMHC$^+$ SMCs; white arrowheads indicate GFP$^+$ ECs without surrounding SMCs. (**H**) Quantification of the percentage of GFP$^+$ ECs among all Cx40$^+$ ECs in the border and infarct regions. Data are presented as mean ± SD; $n = 5$ mice; $^{**}P < 0.01$. (**I**) Sirius Red staining of serial sections of MI hearts. The right panel shows quantification of the scar area. Data are presented as mean ± SD; $n = 5$ mice; n.s., not significant. (**J**) Echocardiography of MI hearts showed no significant difference in ejection fraction and fractional

shortening between control and KDR-overexpression groups. Data are presented as mean ± SD; $n = 5$ mice; n.s., not significant. (**K**) A schematic showing the experimental design. (**L**) Bioluminescence analysis of luciferase activity in mice injected with *Luc* modRNA. (**M**) Whole-mount fluorescence images of hearts injected with *Luc* or *Vegfa* modRNA. Arrowheads indicate GFP$^+$ vessels. (**N**) Immunostaining for GFP, tdT, CD31, and smMHC on heart sections. Yellow arrowheads indicate GFP$^+$ ECs surrounded by smMHC$^+$ SMCs. (**O**) Quantification of the percentage of Cx40$^+$ ECs expressing GFP in the border and infarct regions. Data are presented as mean ± SD; $n = 5$ mice; $^{**}P < 0.01$. (**P**) Echocardiography of MI hearts showed improved ejection fraction and fractional shortening in the *Vegfa* modRNA group. Data are presented as mean ± SD; $n = 5$ mice; $^{*}P < 0.05$. (**Q**) Immunostaining for TNNI3 on MI heart sections. (**R**) Sirius Red staining of serial sections of MI hearts. (**S**) Quantification of the scar area. Data are presented as mean ± SD; $n = 5$ mice; $^{*}P < 0.05$. Scale bars, 1 mm (yellow or black); 100 μm (white).

*Yy1* was deleted (MI-KO mice) 7 days after MI by means of flow cytometry and performed bulk RNA-seq (Fig. 6J). Principal components analysis revealed distinct transcriptomic profiles among the three groups (Fig. 6K). Pathway enrichment analysis showed that genes associated with cell migration, cell proliferation, angiogenesis, VEGF production, and angiogenesis involved in coronary vascular morphogenesis were enriched in MI-WT compared with MI-KO hearts (Fig. 6L). Among the most markedly down-regulated genes in MI-KO ECs was *Hes1*, a key downstream effector of Notch signaling (Fig. 6M), identifying it as a potential YY1-regulated target in the post-MI setting. Given that YY1 was induced by VEGF-A (Fig. 6A), we next asked whether YY1 directly regulates *Hes1* transcription. We treated hESC-ECs with VEGF-A for 48 hours and performed cleavage under targets and release using nuclease (CUT&RUN) sequencing (fig. S12, A and B). CUT&RUN analysis revealed direct YY1 binding at the *HES1* promoter, with prominent peaks near the transcription start site (Fig. 6N). This interaction was further validated with chromatin immunoprecipitation (ChIP)–quantitative polymerase chain reaction (qPCR), which demonstrated enrichment of YY1 at the *HES1* promoter regions (Fig. 6O). Moreover, VEGF-A treatment enhanced YY1 occupancy at these regions (Fig. 6O), suggesting that VEGF-A promotes YY1 recruitment to *HES1* regulatory elements.

We next validated the functional relationship between VEGF-A, YY1, and HES1 in hESC-ECs. Western blot analysis showed that VEGF-A increased both YY1 and HES1 protein expression (fig. S12C). To determine whether YY1 is required for HES1 expression, we performed siRNA-mediated suppression of YY1, which reduced HES1 expression at both the protein and mRNA levels (fig. S12, D to E). Conversely, overexpression of YY1 by modified mRNA (*YY1* modRNA) was sufficient to increase HES1 expression at both the protein and mRNA levels (fig. S12, F to G). To test whether YY1 is required for VEGF-A–induced HES1 up-regulation, we combined YY1 suppression with VEGF-A stimulation. Even in the presence of VEGF-A, YY1 silencing markedly suppressed HES1 expression (fig. S12H). Together, these results demonstrate that YY1 is a critical mediator of VEGF-A–induced *HES1* transcription.

We next investigated the epigenetic mechanism by which YY1 activates *HES1* transcription. H3K4me3 is a well-established histone modification associated with active transcription and is typically enriched at promoters of actively transcribed genes (*51*, *52*). A previous study showed that YY1 promotes H3K4me3 in SMCs (*21*), raising the possibility that a similar mechanism operates in ECs. To test whether YY1 is associated with H3K4me3 in ECs, we performed coimmunoprecipitation (co-IP) assays. Immunoprecipitation of YY1 from hESC-EC lysates followed by immunoblotting revealed association of this activating histone modification (fig. S12I). To further define this mechanism, we examined whether YY1 interacts with methyltransferases responsible for H3K4me3 deposition. H3K4me3 is catalyzed by COMPASS family methyltransferases, with SETD1A and SETD1B serving as major writers at promoter regions (*53*, *54*). Co-IP assays in hESC-ECs revealed that YY1 physically interacts with SETD1A, but not SETD1B, and is also associated with RNA polymerase II (Fig. 6P). These findings suggested that YY1 may selectively recruit SETD1A to target loci to promote transcriptional activation. To test this directly, we performed ChIP-qPCR analysis of the *HES1* promoter. VEGF-A treatment increased H3K4me3 enrichment at the *HES1* promoter (Fig. 6Q), whereas siRNA-mediated suppression of YY1 markedly reduced H3K4me3 at these regions, even in the presence of VEGF-A (fig. S12, J and K). Collectively, these findings establish a VEGF-A–YY1-SETD1A-H3K4me3-HES1 signaling axis in ECs. In this model, VEGF-A induces YY1 expression and promotes its recruitment to the *HES1* promoter, where YY1 interacts with SETD1A to facilitate H3K4 trimethylation, activating *HES1* transcription and promoting coronary collateral formation (Fig. 6R).

## Discussion

Neonatal hearts exhibit a remarkable capacity to regenerate after MI through the de novo formation of collateral arteries, which are essential for restoring blood flow to the infarcted myocardium (*12*, *41*, *55*). The prevailing model for collateral formation is the "artery assembly" concept, which is primarily based on the use of a conventional Tam-induced *Cx40-CreER* lineage-tracing system (*12*). However, our findings challenge this model because we discovered that *Cx40-CreER* also labels a subset of capillary ECs that contribute to collaterals after MI. This observation suggests that Cx40 is not exclusively a marker for preexisting arterial ECs. Additionally, the short washout period between Tam injection and MI complicates the interpretation of lineage tracing. The prolonged presence of Tam in neonates may inadvertently label injury-induced Cx40$^+$ capillary ECs and newly formed collateral ECs expressing Cx40. A critical factor in such experiments is understanding the exact timeline of Tam-induced Cre-*loxP* recombination, which is critical for accurate "pulse-chase" lineage tracing (*16*). If the pulse (P0 to P2) extends into the chase period (P3 to P6), it may continue to label newly generated collateral ECs. Because collaterals begin forming as early as 1 to 2 days after MI (*11*, *12*), this overlap could lead to incorrect conclusions that all labeled cells originate from preexisting arterial ECs during the intended pulse period. To minimize the effects of persistent Tam activity, we developed two intersectional genetic lineage–tracing strategies by combining *Bmx*- and *Cx40*-driven recombinases. Compared with the conventional *Cx40-CreER* system, the marked reduction in tdT$^+$ collateral vessels—labeled only when both *Bmx*- and *Cx40*-driven recombinases are active—in the intersectional approach suggests that many tdT$^+$ collaterals detected in the conventional system likely represent false positives arising from residual Tam activity.

To overcome these limitations, we developed a cell-cell contact-triggered genetic tracing system (*34*, *35*) that is both Tam-independent and free of reliance on arterial EC markers. Using this system, our lineage-tracing data demonstrated that mature arterial ECs modestly contribute to the formation of coronary collaterals after MI. Instead, our interleaved lineage-tracing study reveals that capillaries rather than arterial ECs serve as the principal cellular source of de novo collateral arteries after MI. This process mirrors the developmental program in which capillary ECs coalesce to form coronary artery branches of small diameters during neonatal heart growth (*56*, *57*).

To enhance the arterialization potential of capillaries, we overexpressed *Kdr*, a key regulator of angiogenesis and arterialization (*45*–*48*). After KDR overexpression, a greater number of capillaries expressed Cx40, indicating that Cx40 may also serve as a marker of preartery cells (*58*). However, prolonged activation of VEGF signaling through KDR overexpression failed to promote the formation of functional arteries. Overactivation of VEGF signaling results in the formation of leaky blood vessels, as observed in the tumor vascular bed

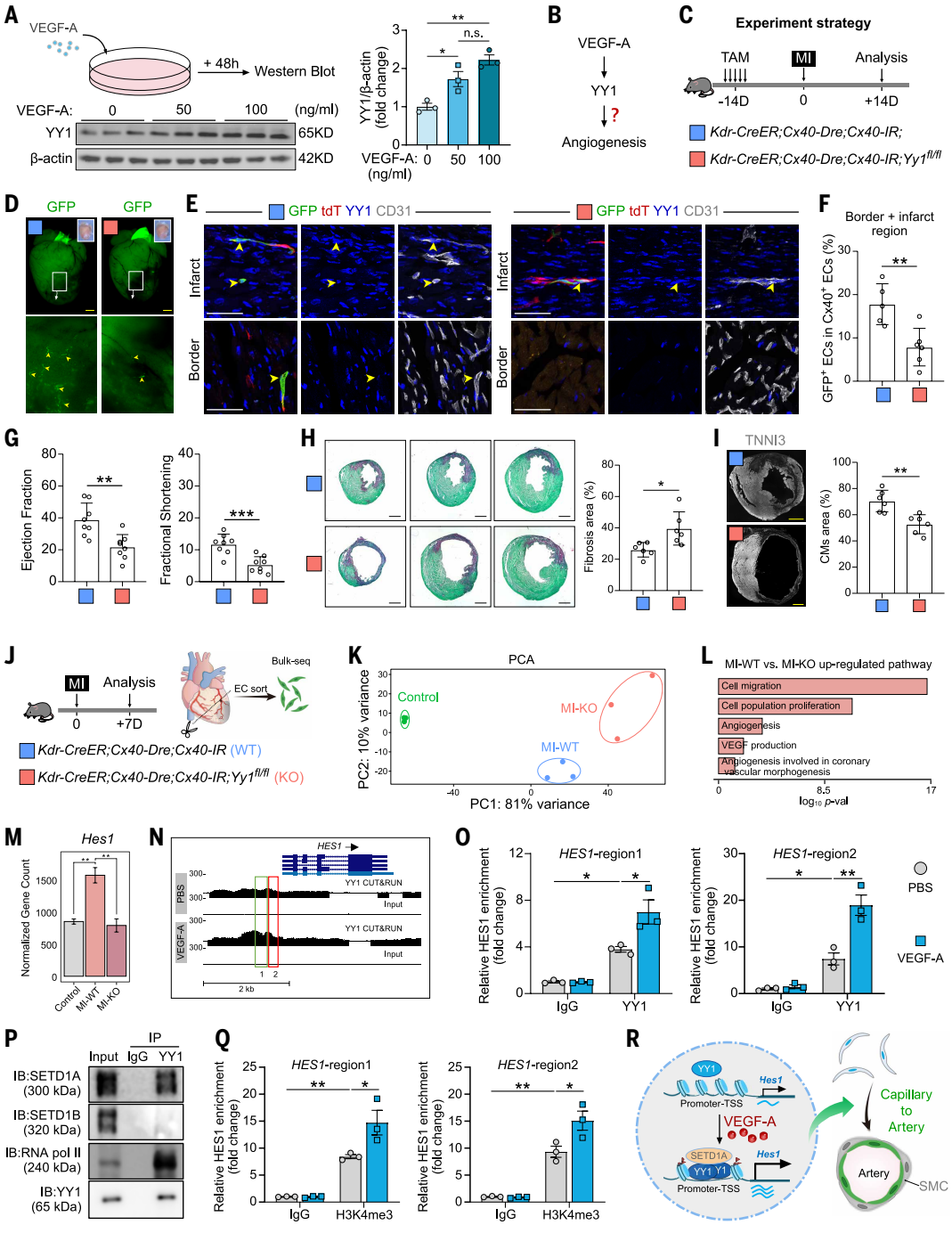


**Fig. 6. VEGF-A regulates HES1 transcription through YY1-mediated H3K4 trimethylation.** (**A**) (Top) A schematic showing the experimental design. (Bottom) Western blot analysis of relative YY1 expression normalized to β-actin in hESC-ECs treated with PBS or VEGF-A. (**B**) The hypothesis of VEGF regulating angiogenesis through YY1. (**C**) A schematic showing the experimental design. (**D**) Whole-mount fluorescence images of control and YY1 KO hearts after MI. Arrowheads indicate $GFP^+$ vessels. (**E**) Immunostaining for GFP, tdT, CD31, and YY1 on heart sections. Yellow arrowheads indicate $GFP^+$ vessels. (**F**) Quantification of the percentage of $Cx40^+$ ECs expressing GFP in the border and infarct regions. Data are presented as mean ± SD; $n = 5$ or 6 mice; $^{**}P < 0.01$. (**G**) Measurement of ejection fraction and fractional shortening by echocardiography of MI hearts. Data are presented as mean ± SD; $n = 8$ mice; $^{**}P < 0.01$, $^{***}P < 0.001$. (**H**) Sirius Red staining of serial sections of MI hearts. (Right) Quantification of the scar area. Data are presented as mean ± SD; $n = 6$ mice; $^{*}P < 0.05$. (**I**) Immunostaining for TNNI3 on MI heart sections. (Right) Quantification of TNNI3 area among ventricular area. Data are presented as mean ± SD; $n = 6$ mice; $^{**}P < 0.01$. (**J**) A schematic showing the experimental design. (**K**) Principal components analysis (PCA) plot of non-MI control (green), MI-WT (blue), and MI-KO (red) cardiac ECs. (**L**) Enriched Gene Ontology (GO) terms among up-regulated genes in MI-WT compared with MI-KO ECs. (**M**) Normalized gene counts of *Hes1* expression across non-MI control, MI-WT, and MI-KO groups. Data are presented as mean ± SEM. (**N**) Visualization of YY1 CUT&RUN in hESC-ECs treated with PBS or VEGF-A, showing the region of *HES1* gene. (**O**) ChIP-qPCR analysis of *HES1* putative promoter region sequence enrichment in hESC-ECs treated with PBS or VEGF-A, immunoprecipitated with IgG or YY1 antibodies. (**P**) Co-IP analysis of SETD1A, SETD1B, and RNA pol II, immunoprecipitated with YY1 antibody in hESC-ECs. (**Q**) ChIP-qPCR analysis of *HES1* putative promoter region sequence enrichment in hESC-ECs treated with PBS or VEGF-A, immunoprecipitated with IgG or H3K4me3 antibodies. (**R**) A cartoon showing the molecular mechanism that regulate capillary-to-collateral formation after MI. Data of hESC-ECs experiments are presented as mean ± SD; $n = 3$ independent cell cultures, $^{**}P < 0.01$, $^{*}P < 0.05$, n.s., not significant. Scale bars, 1 mm (yellow or black); 100 μm (white).

(*59*, *60*). This phenomenon is likely due to abnormal EC proliferation and impaired blood vessel maturation, which compromise vascular stability and functionality. Consistent with this, our data demonstrated that some of these $Cx40^{+}$ ECs were unable to recruit sufficient SMCs and therefore did not acquire the arterial functionality necessary to improve cardiac injury and function. To address this limitation, we used *Vegfa* modRNA to transiently and efficiently activate VEGF signaling in the damaged myocardium. Transient activation of VEGF-A signaling with modRNA has been shown to promote the differentiation of epicardium-derived cells into vascular cells (*49*, *50*). Additionally, moderate VEGF-A supplementation may also restore microcirculatory function, suggesting that targeting the vascular microenvironment represents a valuable therapeutic strategy (*61*–*63*). Our study demonstrated that this transient activation of VEGF-A signaling facilitated the arterialization of capillaries, leading to reduced fibrosis and infarct size, as well as improved cardiac function. Mechanistically, we identified a VEGF-A–YY1–SETD1A–H3K4me3–HES1 signaling axis in ECs that drives the capillary-to-artery transition. Together, our findings establish capillary arterialization as a central mechanism of endogenous cardiac revascularization and identify a molecular pathway that may be leveraged to promote collateral formation and cardiac repair.

## Materials and methods

### Mouse lines and treatments

All mouse studies were conducted in accordance with the guidelines of the Institutional Animal Care and Use Committee at the Center for Excellence in Molecular Cell Science, Shanghai Institutes of Biological Sciences, Chinese Academy of Sciences (CAS). All mice were provided with a standard diet and housed under a 12-hour light-dark cycle. The following mouse lines were used in this study: *Apln-DreER* (*29*), *Cx40-CreER-RFP* (*24*), *R26-RL-GFP* (*30*), *R26-Confetti2* (*64*), *Ki67-LSL-Dre* (*65*), *Cdh5-αGFP-N-tTA* (*35*), *tet-tdT* (*35*), *tet-Dre-BFP* (*35*), *R26-rox-tdT* (*36*), *Cx40-GFP* (*66*), *Cdh5-CreER* (*44*), *NR* (*27*), *R26-tdT* (*40*), *Cx40-Dre* (*17*), *Actb-Cre* (*27*), *H11-Kdr-mCherry* (*67*), *Bmx-CreER* (*33*), and *Cx40-LSL-Dre* (*29*), which have all been reported previously. The following mouse lines were generated using CRISPR/Cas9 technology by Shanghai Model Organisms: *Myh11-mGFP*, *Apln-LSL-Dre*, *Kdr-CreER*, *Cx40-IR*, and *Cx40-IR-DTR*, *Cx40-DreER*, and *H11-ntdT*. For the *Myh11-mGFP* mouse line, the cDNA encoding mGFP was inserted at ATG site in the exon1 of the *Myh11* gene. For the *Apln-LSL-Dre* mouse line, the *loxP-Stop-loxP-Dre-WPRE-polyA* sequence was inserted into exon1 of the *Apln* gene. For the *Kdr-CreER* mouse line, the *P2A-CreER* sequence was inserted between the last coding exon and the 3′ UTR of the *Kdr* gene. For the *Cx40-IR* mouse line, the *loxP-rox-Stop-loxP-GFP-WPRE-polyA-rox-tdT-WPRE-polyA-Frt-Neo-Frt* sequence was inserted into exon2 of the *Cx40* gene. For the *Cx40-IR-DTR* mouse line, the *loxP-rox-Stop-loxP-GFP-2A-diphtheria toxin receptor (DTR)-WPRE-polyA-rox-tdT-WPRE-polyA-Frt-Neo-Frt* sequence was inserted into exon2 of the *Cx40* gene. For the *Cx40-DreER* mouse line, the *DreER* sequence was inserted into exon3 of the *Cx40* gene. For the *H11-ntdT* mouse line, the *loxp-stop-loxp-ntdT* sequence was inserted into *H11* gene locus. The $Yy1^{fl}$ mouse line was generated by placing two loxP sites flanking exon 2 of the *Yy1* gene using CRISPR/Cas9 technology (GemPharmatech). All mouse lines were maintained on a C57BL6/ICR background. The starting time point (Day 0) for each experiment involves adult mice aged 8-12 weeks old. Tamoxifen (Sigma-Aldrich, Cat T5648) was dissolved in corn oil (20 mg/ml) and administered at a dose of 0.2 mg/g body weight per time either by oral gavage at adult time points or by intraperitoneal injection at neonatal time points. Diphtheria toxin (DT, Invitrogen, Cat C10010500BT) was dissolved in PBS and injected intraperitoneally at a dose of 25 ng/g body weight per time at neonatal time points. Doxycycline (Dox, Sigma-Aldrich, Cat D9891) was dissolved in distilled water (2 mg/ml) and provided in the feed water for nursing mothers. Additionally, Dox dissolved in PBS was administered to neonatal mice by intraperitoneal injection at a dose of 0.2 mg/g body weight simultaneously. These procedures ensured precise genetic and pharmacological manipulations for the experiments.

### Genomic PCR

Genomic DNA was extracted from embryonic yolk sacs or mouse tails. The tissues were lysed overnight at 55°C in a lysis buffer containing 100 mM Tris HCl (pH 7.8), 5 mM EDTA, 0.2% SDS, 200 mM NaCl, and 100 mg/ml proteinase K. Following lysis, the mixture was centrifuged at 21130 rcf for 8 min to obtain the supernatant. The supernatant was then precipitated with isopropanol and centrifuged at 21130 rcf for 3 min to isolate genomic DNA pellet. The DNA pellet was washed in 70% ethanol, air-dried, and dissolved in deionized water. All embryos and mice were genotyped with the indicated primers designed to specifically differentiate the targeted sequence from the wild type allele.

### Tissue collecting and whole-mount fluorescence microscopy

The collected tissues were fixed in 4% paraformaldehyde (PFA) at 4°C for 1 hour. After being washed 3 times with PBS, the tissues were placed in dishes containing 1% agarose gel with an appropriate volume of PBS and imaged using an AxioZoom V16 stereo microscope (Zeiss).

### Immunofluorescence staining

The immunostaining protocol was performed as previously reported (*42*). Collected tissues were fixed with 4% PFA at 4°C for 1 hour, followed by three PBS washes and dehydration in 30% sucrose (dissolved in PBS) at 4°C overnight. The tissues were then embedded in OCT (Sakura) and cryo-sectioned into 10 μm frozen sections. The retinas were fixed with 4% PFA at 4°C for 1 hour, followed by three PBS washes and subsequently processed for whole-mount immunostaining. For immunostaining, the sections were dried at room temperature and washed with PBS for three times for 5 min each. The slides or retina were then blocked in 5% PBSST (5% normal donkey serum and 0.02% Triton X-100 in PBS) for 30 min at room temperature. After blocking, the slides were incubated overnight at 4°C with primary antibodies diluted in 2.5% PBSST. The primary used in this study included: smMHC (Abcam, Cat ab224804, 1:300), tdTomato (Rockland, Cat 200-101-379, 1:1000), tdTomato (Rockland, Cat 600-401-379, 1:1000), CD31 (R&D systems, Cat AF3628, 1:300), GFP (Rockland, Cat 600-101-215, 1:500), GFP (Nacalai tesque, Cat 04404-84, 1:500), GFP (Invitrogen, Cat A11122, 1:500), BFP (Evrgen, Cat AB233, 1:500), VE-Cad (R&D systems, Cat AF1002, 1:100), TNNI3 (Abcam, Cat ab56357, 1:200), E-CAD (R&D systems, Cat AF748, 1:500), ZsGreen (Clontech, Cat 632474, 1:2000), αSMA (Abcam, Cat ab5694, 1:100), FABP4 (Abcam, ab13979), YY1 (Abcam, ab109237), Isolectin B4 (vector lab, B-1205). The next day, the slides were washed three times for 5 min each with PBS and incubated for 30 min at room temperature with secondary antibodies and 4'6-diamidino-2-phenylindole (DAPI, Vectorlab, 1:1000) diluted in 0.02% PBST (0.02% Triton X-100 in PBS). Secondary antibodies used included: Donkey anti-rabbit 488 (Invitrogen, Cat A21206, 1:1000), Donkey anti-rabbit 555 (Invitrogen, Cat A31572, 1:1000),Donkey anti-rabbit 647 (Invitrogen, Cat A31573, 1:1000), Donkey anti-goat 488 (Invitrogen, Cat A11055, 1:1000), Donkey anti-goat 555 (Invitrogen, Cat A21432, 1:1000), Donkey anti-goat 647 (Invitrogen, Cat A21447, 1:1000), Donkey anti-rat 594 (JIR, Cat 712-585-153, 1:1000), Donkey anti-rat 488 (Invitrogen, Cat A21208, 1:1000); Donkey anti-rat 647 (Abcam, Cat ab150155, 1:1000), ImmPRESS goat-anti rat (Vector lab, Cat MP-7444; 1:3), ImmPRESS horse anti-rabbit (Vector Laboratories, Cat MP-7401, 1:3), ImmPRESS horse anti-goat (Vector Laboratories, Cat MP-7405, 1:3), HRP-donkey-anti-rat (Jackson ImmunoResearch Inc, Cat 712-035-153,1:100), streptavidin-APC (eBioscience, 17-4317-82). After incubation, the sections or retina were washed and mounted using a mounting medium. Immunostaining images were obtained using a Nikon A1 FLIM, Olympus FV4000, and Zeiss 880 confocal microscope system, and the images were analyzed using ImageJ and Imaris software.

### Neonatal MI model

After being anesthetized on ice, the mouse was placed under a microscope, and a thoracotomy was performed at the 3rd and 4th intercostal spaces to the left of the sternum. The pericardium was carefully incised, and the left anterior descending branch of the coronary artery was ligated using 11-0 nylon sutures. Following the ligation, the chest was closed using 8-0 absorbable sutures.

### Adult MI model

Mice were weighted and anesthetized with isoflurane inhalation. After anesthesia, endotracheal intubation was performed, and the mice were connected to a ventilator. A thoracotomy was conducted at the third and fourth intercostal space to the left of the sternum. The pericardium was opened, and 8-0 nylon sutures were used to ligate the left anterior descending branch of the coronary artery. Successful model replication was confirmed by the left ventricle turned purple. The chest was then closed, and a post-operative intramuscular injection of 20,000 U of penicillin was administered.

### Neonatal apical resections

After being anesthetized on ice, the mouse was placed under a microscope, and a thoracotomy was performed at the third and fourth intercostal space to the left of the sternum. The pericardium was incised, and 0.5 to 1 mm of the apex was resected. The chest was then closed using 8-0 absorbable sutures.

### Sirius Red staining

The assessment of cardiac fibrosis was carried out using Sirius Red staining, following a previously reported procedure (*30*). Heart sections were fixed in 4% PFA for 15 min and subsequently washed three times with PBS, each wash lasting 5 min. The sections were then placed in Bouin solution, composing of 9% formaldehyde, 5% acetic acid, and 0.9% picric acid, for prolonged fixation over 24 hours. On the following day, the sections were rinsed with tap water and incubated in a 0.1% Fast Green solution (Thermo Fisher Scientific) for 5 min. After incubation, the sections were rinsed with tap water, followed by a 1-min incubation in 1% acetic acid. They were then washed with distilled water and incubated in a 0.1% Sirius Red solution for 2 min. After this staining step, the sections were washed again with distilled water. For dehydration, the sections were sequentially immersed in 95% ethanol, 100% ethanol, and xylene, with each step lasting 5 min and repeated twice. Finally, the sections were mounted using a resin-based mounting medium. Images of the stained sections were captured using an Olympus microscope (model BX53).

### Echocardiography

Two weeks following MI, the geometry and function of the left ventricle were assessed using the high-resolution Vevo 3100 transthoracic echocardiography system (VisualSonics). M-mode ultrasound imaging was performed through a parasternal long-axis view, capturing images at the level of the papillary muscle and midway between the papillary muscle and the apex. Ejection fractions were calculated using the Vevo Lab 3.2.7 software package.

### Whole mount immunostaining and confocal imaging of neonatal hearts

The neonatal mouse heart whole mount immunostaining was performed following a previously reported procedure (*12*). Briefly, hearts were fixed in 4% PFA for 1 hour at 4°C, followed by three 10-min washes with PBS. The hearts were then incubated with primary antibodies diluted in 0.5% PBST (PBS containing 0.5% Triton X-100) for 24 hours at 4°C. After primary antibody incubation, the hearts were washed in 0.5% PBST for 24 hours at 4°C, with the washing solution changed six times during this period. Subsequently, the hearts were incubated with secondary antibodies diluted 1:250 in 0.5% PBST overnight at 4°C. Following secondary antibody incubation, the hearts were washed again in 0.5% PBST for 24 hours at 4°C, with six solution changes. All steps were carried out with gentle and continuous shaking. After completing the immunostaining process, the hearts were cleared with Vectashield (Vector; Cat: H-100) for 2 hours at room temperature (RT). The hearts were then flattened between a double concave microscope slide (Sail brand; Cat: 7104) and a thick microscope coverslip. Imaging was performed using a Zeiss 880 or Olympus FV4000 confocal microscope.

### Synthesis of modRNA and modRNA transfection

The synthesis of modified mRNA (modRNA) was performed as described previously (*49*). Briefly, open reading frames (ORFs) were amplified by PCR from plasmids encoding luciferase and mouse VEGF-A, which were then used to template Poly A tail PCRs. RNA was synthesized with the MEGAscript T7 kit (Ambion) with a custom ribonucleoside blend. This blend included 3′-O-Me-m7G(5′)ppp(5′)G cap analog (New England Biolabs), ATP, guanosine triphosphate (USB), 5-methylcytidine triphosphate, and pseudouridine triphosphate (TriLink Biotechnologies). The synthesized RNA was purified using Ambion MEGAclear spin columns and treated with Antarctic Phosphatase (New England Biolabs) for 1 hour at 37°C to remove residual 5′-phosphates. After enzymatic treatment, the RNA was repurified, quantified by a Nanodrop spectrophotometer (Thermo Scientific), and precipitated with 5M ammonium acetate according to the manufacturer's instructions. The modRNA was resuspended in elution buffer, stored at -80°C, and prepared for in vivo use. To create the transfection mixture, modRNA and in vivo-jetRNA$^{+}$ (Polyplus, Cat: 101000122) were combined and incubated for 15 min at RT according to the manufacturer's instructions. The transfection mixture was then injected directly into the cardiac muscle. For visualization of the luciferase bioluminescent signal, luciferin (150 μg/g body weight; Sigma) was injected intraperitoneally. After 10 min, mice were anesthetized with isoflurane and imaged using the PerkinElmer IVIS Lumina III system. Imaging data were analyzed and quantified using Living Image Software, with the signal strength visualized using a spectrum of 12 different colors.

### Vascular perfusion measure

For lectin perfusion, Isolectin B4-649 (Vector Laboratories, DL-1208) was administered via tail vein injection in adult mice at a dose of 6.25 μl per gram body weight, and via the vena cava in neonatal mice at 50 μl per animal 2 hours prior to euthanasia. Microfil perfusion was performed to assess coronary artery perfusion, as previously described (*68*). Briefly, mice were intraperitoneally injected with heparin solution (1:10 in PBS) for 5 min. The mice were then euthanized, the thoracic cavity was opened, and the vasculature was perfused sequentially with 1× PBS followed by 4% paraformaldehyde (PFA). Microfil (Flow Tech) was subsequently injected via the thoracic aorta until the arterial circulation was fully filled. After polymerization of Microfil for 60 min, hearts were dissected and fixed in 4% PFA at 4°C overnight. The following day, hearts were washed three times in PBS (5 min each) and cleared in methyl salicylate for several days. Cleared hearts were then imaged using micro–computed tomography (SkyScan 1272).

### Coronary EC sorting

Coronary ECs were sorted as previously described (*15*). Neonatal and adult mouse hearts were dissected for tissue dissociation, and atria were removed from each heart. For postnatal day 2 (P2) mice, approximately six hearts were pooled per sample for cell sorting. For adult MI hearts, the infarct and border regions were collected for digestion. Tissues were digested in buffer containing 500 U/ml Collagenase IV, 1.2 U/ml Dispase, and 32 U/ml DNase I in HBSS. Each neonatal heart was transferred into 300 μl of digestion buffer, whereas each adult heart was transferred into 1 ml of digestion buffer. Samples were incubated at 37°C for 45 min with gentle agitation. Digestion was

terminated by adding PBS containing 5% fetal bovine serum (FBS), followed by filtration through a 40-μm sterile cell strainer. Cells were then centrifuged at 400 × g for 5 min at 4°C, and the pellet was resuspended in 600 μl PBS containing 3% FBS. Single-cell suspensions from neonatal hearts were stained with CD31–PE-Cy7 and CD45–APC, whereas cells from adult hearts were stained with CD31–APC for 30 min at 4°C. Cells were washed and resuspended in fresh PBS containing 3% FBS, followed by fluorescence-activated cell sorting (FACS). DAPI was added immediately before sorting to exclude dead cells. Neonatal endothelial cells (ECs, $DAPI^-$ $CD45^-$ $CD31^+$) were sorted using a Sony MA900 cell sorter for subsequent single-cell RNA sequencing, whereas adult ECs ($DAPI^-$ $CD31^+$) were collected for bulk RNA sequencing or RT-qPCR.

### Single-cell library preparation

FACS-sorted cells were subjected to 5′ transcriptomic analysis using the Chromium Next GEM Single Cell 5′ Reagent Kit (v3 Chemistry). After generating GEMs on a 10x Chromium Controller, cDNA was amplified and converted into sequencing libraries according to standard manufacturer guidelines. Sequencing was performed on an Illumina NovaSeq 6000 (PE150) to achieve a comprehensive transcriptional readout.

### Single-cell transcriptomic data processing and analysis

Initial quality control and adapter removal of raw sequencing data were conducted using Trim Galore (v0.6.7), applying a quality threshold of 20 and a stringency of 13 for paired-end reads. Only sequences with a minimum length of 150 bp were retained. Subsequently, the high-quality reads were mapped to a tailored mm10 mouse reference genome utilizing the count function of Cell Ranger (v6.1.1) under default configurations to produce the final gene expression matrices.

Downstream analysis was performed using the Seurat (v4.1.2) package in R. Initial Seurat objects were created by filtering out genes expressed in fewer than 3 cells and cells expressing fewer than 200 genes. To ensure high-quality transcriptomic data, cells were retained based on the following criteria: a minimum of 1000 detected genes and a mitochondrial gene content of less than 10%.

To focus our analysis on endothelial lineages and their specific subpopulations, we curated a comprehensive suite of gene signatures (*69*). Principal Component Analysis (PCA) was performed using a restricted feature space defined by these curated endothelial gene signatures. Clustering was executed using a shared nearest neighbor (SNN) modularity optimization-based algorithm with a resolution of 1.8. Outlier clusters were identified and removed to refine the cell population for downstream analysis. To facilitate comparative analysis between IGT and WT samples, the two datasets were integrated using the standard integration workflow in Seurat. A set of 2000 integration anchors was identified following canonical correlation analysis (CCA). The integrated dataset was then scaled, and a joint PCA was performed using the predefined endothelial signatures. For visualization, the high-dimensional data were projected into a two-dimensional (2D) space using uniform manifold approximation and projection (UMAP) based on the first 30 principal components. To investigate the developmental dynamics and lineage specification of the endothelial populations, we performed diffusion map dimensionality reduction and diffusion pseudotime (DPT) estimation. These analyses were executed using the destiny (v3.20.0) R package.

### RNA-seq data analysis

High-quality paired-end reads were aligned to the mouse reference genome using HISAT2 (v2.2.1). Gene counts were quantified using HTSeq (v2.0.1) to generate a comprehensive expression matrix. Downstream transcriptomic analysis was performed using the DESeq2 (v1.46.0) R package. To visualize sample relationships, Principal Component Analysis (PCA) was subsequently performed on the top 3,000 most variable genes to assess the global transcriptional variance across groups. Differentially expressed genes (DEGs) were identified based on an adjusted p-value threshold of 0.05 and a minimum absolute log2 fold-change of 0.5. Functional implications were further explored through Gene Ontology (GO) enrichment analysis using the limma (v3.62.1) R package, with all detected genes serving as the background.

### hESC-EC differentiation

The H9 hESC line (WiCell, WA09) was maintained in mTesR1 medium (StemCell Technologies, Cat No. 85850). hESC-ECs were differentiated from hESCs under defined conditions as previously described (*70*). Briefly, hESC were cultured in mesoderm differentiation medium containing 50% DMEM/F12-Glutamax and 50% neurobasal media supplemented with 1% N2, 2% B27, 50 μM 2-mercaptoethanol and 2 mM L-glutamine (Gibco). Growth factors and small molecules including 25 ng/ml BMP4 (Peprotech, Cat No. AF-120-05ET) and 8 μM CHIR99021 (Selleck Chem, Cat No. S2924) were added to the mesoderm differentiation medium from day 1 to day 4. From day 4 onwards, hESC were cultured in EC differentiation medium containing StemPro medium (Gibco, Cat No. 10639011) supplemented with 200 ng/ml VEGF-A (Perprotech, Cat No. 100-20) and 2 μM forsokolin (Abcam, Cat No. ab120058). At day 6, differentiated hESC-ECs were dissociated by TrypLE Express (Thermo Fisher, Cat No. 12604021) then purified with CD144 MicroBeads (Miltenyi Biotec, Cat no. 130-097-857) and maintained in EGM-2 medium (Lonza, Cat No. CC-3162). In some experiments, hESC-ECs were treated with PBS (control), 50 ng/ml or 100 ng/ml VEGF-A for 48 hours (Perprotech, Cat No. 100-20) prior to further analysis.

### Western blot analysis

Total proteins from hESC-ECs were extracted using RIPA lysis buffer (Beyotime, Cat. No. P0013B) supplemented with a protease inhibitor cocktail (MedChemExpress, Cat. No. HY-K0011) on ice for 30 min and centrifuged at 13,000 rpm for 5 min at 4°C. The concentration of total protein was determined using a BCA Protein Assay Kit (Thermo Scientific, Cat. No. 23225). The lysate was mixed with SDS-PAGE sample loading buffer (Beyotime, Cat. No. P0015F) and boiled at 100°C for 5 min. Equal amounts (30 μg) of protein samples were separated by 6-10% standard sodium dodecyl sulfate-polyacrylamide gel electrophoresis (SDS-PAGE) and subsequently transferred to a polyvinylidene difluoride (PVDF) membrane with a pore size of 0.2 μm (Roche, Cat. No. 03010040001). The membranes were blocked in 5% skim milk (dissolved in TBST) for 1 hour at room temperature and incubated with primary antibodies (1:1000 dilution) overnight at 4°C. After washing three times with TBST, the membranes were incubated with corresponding anti-mouse or anti-rabbit horseradish peroxidase (HRP)-conjugated secondary antibodies (1:5000 dilution) for 1 hour at room temperature. Immunoreactive bands were visualized using a chemiluminescent substrate (Thermo Scientific, Cat. No. 34095) with a chemiluminescence imaging system (Syngene, GeneGnome XRQ). Protein expression was measured by analyzing the integral optical density (IOD) of the protein bands using Image-Pro Plus software. Antibodies used for Western blot analysis in this study are listed in table S1.

### Co-IP

Co-IP was performed using protein A/G magnetic beads (Thermo Scientific, Cat. No. 88803) according to the manufacturer's instructions. In brief, total protein was extracted from hESC-ECs using RIPA lysis buffer (Beyotime, Cat. No. P0013B) supplemented with protease inhibitor cocktail (MedChemExpress, Cat. No. HY-K0011) on ice for 30 min and centrifuged at 13,000 rpm for 5 min at 4°C. 2% total protein lysates were used as input, and the remaining lysate was pre-cleared by incubation with 30 μl of protein A/G beads at 4°C for 30 min to remove nonspecifically binding proteins. After bead removal, 2 μg of specific target antibody or control immunoglobulin G (IgG) antibody were

added to 1 mg of protein lysates, followed by gentle rotation at 4°C overnight. Subsequently, 30 μl of protein A/G beads were added to the sample lysates and incubated at 4°C for 4 hours. The beads were then washed with washing buffer for three times. After elution from the protein A/G beads using elution buffer, the input and immunoprecipitated samples were mixed with SDS-PAGE sample loading buffer (Beyotime, Cat. No. P0015F), boiled at 100°C for 5 min, and subsequently subjected to Western blot analysis. Antibodies used for Co-IP analysis in this study are listed in table S1.

### RT-qPCR

Total RNA was extracted from hESC-ECs or ECs sorted from hearts using TRIzol reagent (Vazyme, Cat. No. R401-01) according to the manufacturer's instructions. The concentration and purity of RNA samples were quantified using a Nanodrop 2000 (Thermo Fisher). An equal amount of total RNA (1 μg) was used for reverse-transcription polymerase chain reaction to synthesize the first strand of cDNA with a cDNA Synthesis Kit (Bio-Rad, Cat. No. 1708890). RT-qPCR was performed using the CFX Connect Real-Time PCR Detection System (Bio-Rad) with SYBR Green Supermix (Bio-Rad, Cat. No. 1725122). The fold change in gene expression was calculated using the $2^{-\Delta\Delta Ct}$ method, and the relative gene expression levels were normalized to the internal control gene β-*actin (Actb)*. The primers used are listed in table S2.

### CUT&RUN sequencing

CUT&RUN was performed on hESC-ECs using the CUT&RUN assay kit (Cell Signaling Technology, Cat. No. 86652) according to the manufacturer's instructions. Briefly, $1 \times 10^5$ live hESC-ECs were harvested, washed, and bound to concanavalin A-coated magnetic beads to immobilize the cells. Bead-bound cells were then permeabilized and incubated with a primary antibody specific to the target protein at 4°C overnight with gentle agitation. After washing to remove unbound antibody, cells were incubated with a recombinant pAG-MNase enzyme for 1 hour at 4°C to tether the nuclease to the antibody-bound chromatin. Targeted chromatin cleavage was initiated by the addition of calcium chloride and carried out at 4°C for 30 min. The reaction was stopped by adding stop buffer, and the released chromatin fragments were collected from the supernatant. The input control sample (antibody untreated) was processed in parallel to assess background cleavage and to normalize signal enrichment. DNA was purified using spin columns provided in the kit and sequencing libraries were prepared according to the instructions of the DNA Library Prep Kit for Illumina (New England Biolabs, Cat. No. E7645). Sequencing was performed in a paired-end 150 bp configuration on the Illumina NovaSeq system, following manufacturer's instructions. The antibodies used in CUN&RUN assay are listed in table S1.

### CUT&RUN sequencing analysis

The sequenced reads were aligned to the human reference genome with the annotated gene model (GRCh38, GENCODE) using the Burrow-Wheeler Aligner (version 0.7.19) with the Maximum Exact Match algorithm. After filtering out GRCh38 ENCODE blacklisted regions and removing duplicate reads, peaks were identified using the Model-Based Analysis of ChIP-Seq peak caller (MACS; version 2.2.9.1; pypi.org/project/MACS2/) with a *q* value cutoff of 0.01. Annotation of peaks was performed with the Hypergeometric Optimization of Motif Enrichment (HOMER) software (version 5.1; homer.ucsd.edu/homer/) and the annotated gene model (GRCh38, GENCODE). With default settings, peaks were assigned to the nearest transcription start site (TSS) of genes, and further classified using the following features: TSS (−1 kb to +100 bp), transcription termination site (TTS) (−100 bp to +1kb), exons, introns, and intergenic regions. Heat map visualization was performed using deepTools (version 3.5.6; github.com/deeptools/deepTools). Selected genes with YY1 binding peaks were visualized using the UCSC (University of California, Santa Cruz) genome browser.

### ChIP assay

ChIP assays were performed in hESC-ECs with a SimpleChIP Enzymatic Chromatin IP Kit (Cell Signaling Technology, Cat. No. 9003) according to the manufacturer's instructions. In brief, the hESC-ECs were cross-linked with 1% formaldehyde (Sigma) at room temperature for 10 min. The reaction was quenched by the addition of 0.125 M glycine and incubate at room temperature for 5 min. The cross-linked chromatin was then fragmented using 0.5 μl of micrococcal nuclease for 20 min at 37°C, followed by 3 sets of 20 s of sonication (Shanghai Lichen Bangxi Technology Co.) to break nuclear membrane. 2% of the cross-linked chromatin was taken as input, and 2 μg of either the immunoprecipitating or IgG antibody was added to chromatin samples, which were then incubated with rotation at 4°C overnight. Subsequently, protein G magnetic beads were added to the reaction samples and incubated for 2 hours at 4°C with rotation. The protein G magnetic beads were then washed three times with low salt buffer and once with high salt buffer. Elution buffer was added to each ChIP sample to elute the chromatin from the antibody/protein G magnetic beads. For the input and ChIP samples, 6 μl of 5 M Nacl and 2 μl of Proteinase K were added and incubated for 2 hours at 65°C. The DNA was further purified using DNA purification spin columns. The immunoprecipitating antibodies used in ChIP are listed in table S1. For ChIP-qPCR, the precipitated genomic DNA was resuspended in 50 μl of DNA Elution Buffer and then diluted to a total volume of 200 μl. The ChIP DNA was analyzed by qPCR using specific primers targeting the *HES1* promoter region, and the data were normalized to the input DNA. The primers used in ChIP-qPCR are listed in table S3.

### Quantification and statistical analysis

The heart samples were blinded and randomized for analysis, with no fewer than 5 biological samples collected for each mouse group in each experiment. Quantification data were presented as mean ± standard deviation (SD). Statistical comparisons between two groups were performed using the unpaired two-tailed Student's *t* test, while comparisons among multiple groups were conducted using ANOVA followed by Tukey's method. A $P$ value $< 0.05$ was regarded as statistically significant.

### REFERENCES AND NOTES


1. S. S. Martin *et al.*, 2024 heart disease and stroke statistics: A report of US and global data from the American Heart Association. *Circulation* **149**, e347–e913 (2024). doi: 10.1161/CIR.0000000000001209; pmid: 38264914
2. C. Seiler, M. Stoller, B. Pitt, P. Meier, The human coronary collateral circulation: Development and clinical importance. *Eur. Heart J.* **34**, 2674–2682 (2013). doi: 10.1093/eurheartj/eht195; pmid: 23739241
3. D. E. Gregg, The natural history of coronary collateral development. *Circ. Res.* **35**, 335–344 (1974). doi: 10.1161/01.RES.35.3.335; pmid: 4608623
4. W. Schaper, W. D. Ito, Molecular mechanisms of coronary collateral vessel growth. *Circ. Res.* **79**, 911–919 (1996). doi: 10.1161/01.RES.79.5.911; pmid: 8888683
5. A. Helisch, W. Schaper, Arteriogenesis: The development and growth of collateral arteries. *Microcirculation* **10**, 83–97 (2003). doi: 10.1080/mic.10.1.83.97; pmid: 12610665
6. C. Seiler, P. Meier, Historical aspects and relevance of the human coronary collateral circulation. *Curr. Cardiol. Rev.* **10**, 2–16 (2014). doi: 10.2174/1573403X113099990028; pmid: 23859295
7. P. J. Sabia *et al.*, An association between collateral blood flow and myocardial viability in patients with recent myocardial infarction. *N. Engl. J. Med.* **327**, 1825–1831 (1992). doi: 10.1056/NEJM199212243272601; pmid: 1448120
8. F. Mac Gabhann, S. M. Peirce, Collateral capillary arterialization following arteriolar ligation in murine skeletal muscle. *Microcirculation* **17**, 333–347 (2010). doi: 10.1111/j.1549-8719.2010.00034.x; pmid: 20618691
9. J. E. Faber, W. M. Chilian, E. Deindl, N. van Royen, M. Simons, A brief etymology of the collateral circulation. *Arterioscler. Thromb. Vasc. Biol.* **34**, 1854–1859 (2014). doi: 10.1161/ATVBAHA.114.303929; pmid: 25012127
10. M. Simons, A. Eichmann, Molecular controls of arterial morphogenesis. *Circ. Res.* **116**, 1712–1724 (2015). doi: 10.1161/CIRCRESAHA.116.302953; pmid: 25953926
11. H. Zhang, J. E. Faber, De-novo collateral formation following acute myocardial infarction: Dependence on CCR2$^+$ bone marrow cells. *J. Mol. Cell. Cardiol.* **87**, 4–16 (2015). doi: 10.1016/j.yjmcc.2015.07.020; pmid: 26254180

12. S. Das *et al.*, A unique collateral artery development program promotes neonatal heart regeneration. *Cell* **176**, 1128–1142.e18 (2019). doi: 10.1016/j.cell.2018.12.023; pmid: 30686582
13. A. Jamaiyar *et al.*, The essential role for endothelial cell sprouting in coronary collateral growth. *J. Mol. Cell. Cardiol.* **165**, 158–171 (2022). doi: 10.1016/j.yjmcc.2022.01.005; pmid: 35074317
14. L. He *et al.*, Genetic lineage tracing discloses arteriogenesis as the main mechanism for collateral growth in the mouse heart. *Cardiovasc. Res.* **109**, 419–430 (2016). doi: 10.1093/cvr/cvw005; pmid: 26768261
15. G. Arolkar *et al.*, Dedifferentiation and proliferation of artery endothelial cells drive coronary collateral development in mice. *Arterioscler. Thromb. Vasc. Biol.* **43**, 1455–1477 (2023). doi: 10.1161/ATVBAHA.123.319319; pmid: 37345524
16. R. B. Reinert *et al.*, Tamoxifen-induced Cre-loxP recombination is prolonged in pancreatic islets of adult mice. *PLOS ONE* **7**, e33529 (2012). doi: 10.1371/journal.pone.0033529; pmid: 22470452
17. M. Han *et al.*, Dual genetic lineage tracing reveals capillary to artery formation in the adult heart. *Circulation* **145**, 1179–1181 (2022). doi: 10.1161/CIRCULATIONAHA.121.056249; pmid: 35404681
18. H. W. Jeong *et al.*, Transcriptional regulation of endothelial cell behavior during sprouting angiogenesis. *Nat. Commun.* **8**, 726 (2017). doi: 10.1038/s41467-017-00738-7; pmid: 28959057
19. Y. Shi, E. Seto, L. S. Chang, T. Shenk, Transcriptional repression by YY1, a human GLI-Krüppel-related protein, and relief of repression by adenovirus E1A protein. *Cell* **67**, 377–388 (1991). doi: 10.1016/0092-8674(91)90189-6; pmid: 1655281
20. S. Gordon, G. Akopyan, H. Garban, B. Bonavida, Transcription factor YY1: Structure, function, and therapeutic implications in cancer biology. *Oncogene* **25**, 1125–1142 (2006). doi: 10.1038/sj.onc.1209080; pmid: 16314846
21. W. Ye *et al.*, YY1 regulates vascular resistance and blood pressure dynamics through epigenetic control of m6A RNA modifications in vascular smooth muscle cells. *Cardiovasc. Res.* **121**, 1898–1916 (2025). doi: 10.1093/cvr/cvaf136; pmid: 40795179
22. Z. J. Liu *et al.*, Regulation of Notch1 and Dll4 by vascular endothelial growth factor in arterial endothelial cells: Implications for modulating arteriogenesis and angiogenesis. *Mol. Cell. Biol.* **23**, 14–25 (2003). doi: 10.1128/MCB.23.1.14-25.2003; pmid: 12482957
23. C. Roca, R. H. Adams, Regulation of vascular morphogenesis by Notch signaling. *Genes Dev.* **21**, 2511–2524 (2007). doi: 10.1101/gad.1589207; pmid: 17938237
24. S. Beyer, R. G. Kelly, L. Miquerol, Inducible Cx40-Cre expression in the cardiac conduction system and arterial endothelial cells. *Genesis* **49**, 83–91 (2011). doi: 10.1002/dvg.20687; pmid: 21344610
25. L. Miquerol *et al.*, Endothelial plasticity drives arterial remodeling within the endocardium after myocardial infarction. *Circ. Res.* **116**, 1765–1771 (2015). doi: 10.1161/CIRCRESAHA.116.306476; pmid: 25834185
26. B. Sharma, A. Chang, K. Red-Horse, Coronary artery development: Progenitor cells and differentiation pathways. *Annu. Rev. Physiol.* **79**, 1–19 (2017). doi: 10.1146/annurev-physiol-022516-033953; pmid: 27959616
27. L. He *et al.*, Enhancing the precision of genetic lineage tracing using dual recombinases. *Nat. Med.* **23**, 1488–1498 (2017). doi: 10.1038/nm.4437; pmid: 29131159
28. Q. Liu *et al.*, Genetic targeting of sprouting angiogenesis using Apln-CreER. *Nat. Commun.* **6**, 6020 (2015). doi: 10.1038/ncomms7020; pmid: 25597280
29. X. Han *et al.*, A suite of new Dre recombinase drivers markedly expands the ability to perform intersectional genetic targeting. *Cell Stem Cell* **28**, 1160–1176.e7 (2021). doi: 10.1016/j.stem.2021.01.007; pmid: 33567267
30. M. Han *et al.*, Dual genetic tracing reveals a unique fibroblast subpopulation modulating cardiac fibrosis. *Nat. Genet.* **55**, 665–678 (2023). doi: 10.1038/s41588-023-01337-7; pmid: 36959363
31. A. Álvarez-Aznar *et al.*, Tamoxifen-independent recombination of reporter genes limits lineage tracing and mosaic analysis using CreER$^{T2}$ lines. *Transgenic Res.* **29**, 53–68 (2020). doi: 10.1007/s11248-019-00177-8; pmid: 31641921
32. L. Madisen *et al.*, Transgenic mice for intersectional targeting of neural sensors and effectors with high specificity and performance. *Neuron* **85**, 942–958 (2015). doi: 10.1016/j.neuron.2015.02.022; pmid: 25741722
33. M. Ehling, S. Adams, R. Benedito, R. H. Adams, Notch controls retinal blood vessel maturation and quiescence. *Development* **140**, 3051–3061 (2013). doi: 10.1242/dev.093351; pmid: 23785053
34. L. Morsut *et al.*, Engineering customized cell sensing and response behaviors using synthetic notch receptors. *Cell* **164**, 780–791 (2016). doi: 10.1016/j.cell.2016.01.012; pmid: 26830878
35. S. Zhang *et al.*, Monitoring of cell-cell communication and contact history in mammals. *Science* **378**, eabo5503 (2022). doi: 10.1126/science.abo5503; pmid: 36454848
36. H. Zhang *et al.*, Genetic lineage tracing identifies endocardial origin of liver vasculature. *Nat. Genet.* **48**, 537–543 (2016). doi: 10.1038/ng.3536; pmid: 27019112
37. K. E. Kim, H. K. Sung, G. Y. Koh, Lymphatic development in mouse small intestine. *Dev. Dyn.* **236**, 2020–2025 (2007). doi: 10.1002/dvdy.21200; pmid: 17576138
38. A. I. McDonald *et al.*, Endothelial regeneration of large vessels is a biphasic process driven by local cells with distinct proliferative capacities. *Cell Stem Cell* **23**, 210–225.e6 (2018). doi: 10.1016/j.stem.2018.07.011; pmid: 30075129
39. Y. Li *et al.*, Dynamics of endothelial cell generation and turnover in arteries during homeostasis and diseases. *Circulation* **149**, 135–154 (2024). doi: 10.1161/CIRCULATIONAHA.123.064301; pmid: 38084582
40. L. Madisen *et al.*, A robust and high-throughput Cre reporting and characterization system for the whole mouse brain. *Nat. Neurosci.* **13**, 133–140 (2010). doi: 10.1038/nn.2467; pmid: 20023653
41. E. R. Porrello *et al.*, Regulation of neonatal and adult mammalian heart regeneration by the miR-15 family. *Proc. Natl. Acad. Sci. U.S.A.* **110**, 187–192 (2013). doi: 10.1073/pnas.1208863110; pmid: 23248315
42. X. Tian *et al.*, Subepicardial endothelial cells invade the embryonic ventricle wall to form coronary arteries. *Cell Res.* **23**, 1075–1090 (2013). doi: 10.1038/cr.2013.83; pmid: 23797856
43. X. Tian *et al.*, Vessel formation. De novo formation of a distinct coronary vascular population in neonatal heart. *Science* **345**, 90–94 (2014). doi: 10.1126/science.1251487; pmid: 24994653
44. K. Liu *et al.*, Lineage tracing clarifies the cellular origin of tissue-resident macrophages in the developing heart. *J. Cell Biol.* **221**, e202108093 (2022). doi: 10.1083/jcb.202108093; pmid: 35482005
45. N. D. Lawson, A. M. Vogel, B. M. Weinstein, sonic hedgehog and vascular endothelial growth factor act upstream of the Notch pathway during arterial endothelial differentiation. *Dev. Cell* **3**, 127–136 (2002). doi: 10.1016/S1534-5807(02)00198-3; pmid: 12110173
46. B. Wu *et al.*, Endocardial cells form the coronary arteries by angiogenesis through myocardial-endocardial VEGF signaling. *Cell* **151**, 1083–1096 (2012). doi: 10.1016/j.cell.2012.10.023; pmid: 23178125
47. W. Luo *et al.*, Arterialization requires the timely suppression of cell growth. *Nature* **589**, 437–441 (2021). doi: 10.1038/s41586-020-3018-x; pmid: 33299176
48. X. Tian, B. Zhou, Coronary vessel formation in development and regeneration: Origins and mechanisms. *J. Mol. Cell. Cardiol.* **167**, 67–82 (2022). doi: 10.1016/j.yjmcc.2022.03.009; pmid: 35354073
49. L. Zangi *et al.*, Modified mRNA directs the fate of heart progenitor cells and induces vascular regeneration after myocardial infarction. *Nat. Biotechnol.* **31**, 898–907 (2013). doi: 10.1038/nbt.2682; pmid: 24013197
50. L. Carlsson *et al.*, Biocompatible, purified *VEGF-A* mRNA improves cardiac function after intracardiac injection 1 week post-myocardial infarction in swine. *Mol. Ther. Methods Clin. Dev.* **9**, 330–346 (2018). doi: 10.1016/j.omtm.2018.04.003; pmid: 30038937
51. D. Schübeler *et al.*, The histone modification pattern of active genes revealed through genome-wide chromatin analysis of a higher eukaryote. *Genes Dev.* **18**, 1263–1271 (2004). doi: 10.1101/gad.1198204; pmid: 15175259
52. B. E. Bernstein *et al.*, A bivalent chromatin structure marks key developmental genes in embryonic stem cells. *Cell* **125**, 315–326 (2006). doi: 10.1016/j.cell.2006.02.041; pmid: 16630819
53. A. Shilatifard, The COMPASS family of histone H3K4 methylases: Mechanisms of regulation in development and disease pathogenesis. *Annu. Rev. Biochem.* **81**, 65–95 (2012). doi: 10.1146/annurev-biochem-051710-134100; pmid: 22663077
54. J. H. Lee, D. G. Skalnik, CpG-binding protein (CXXC finger protein 1) is a component of the mammalian Set1 histone H3-Lys4 methyltransferase complex, the analogue of the yeast Set1/COMPASS complex. *J. Biol. Chem.* **280**, 41725–41731 (2005). doi: 10.1074/jbc.M508312200; pmid: 16253997
55. A. B. Aurora *et al.*, Macrophages are required for neonatal heart regeneration. *J. Clin. Invest.* **124**, 1382–1392 (2014). doi: 10.1172/JCI72181; pmid: 24569380
56. X. Tian *et al.*, Peritruncal coronary endothelial cells contribute to proximal coronary artery stems and their aortic orifices in the mouse heart. *PLOS ONE* **8**, e80857 (2013). doi: 10.1371/journal.pone.0080857; pmid: 24278332
57. J. Tang *et al.*, Extension of endocardium-derived vessels generate coronary arteries in neonates. *Circ. Res.* **130**, 352–365 (2022). doi: 10.1161/CIRCRESAHA.121.320335; pmid: 34995101
58. T. Su *et al.*, Single-cell analysis of early progenitor cells that build coronary arteries. *Nature* **559**, 356–362 (2018). doi: 10.1038/s41586-018-0288-7; pmid: 29973725
59. P. Carmeliet, Angiogenesis in life, disease and medicine. *Nature* **438**, 932–936 (2005). doi: 10.1038/nature04478; pmid: 16355210
60. P. Carmeliet, R. K. Jain, Molecular mechanisms and clinical applications of angiogenesis. *Nature* **473**, 298–307 (2011). doi: 10.1038/nature10144; pmid: 21593862
61. M. Grunewald *et al.*, Counteracting age-related VEGF signaling insufficiency promotes healthy aging and extends life span. *Science* **373**, eabc8479 (2021). doi: 10.1126/science.abc8479; pmid: 34326210
62. G. Luxán, S. Dimmeler, The vasculature: A therapeutic target in heart failure? *Cardiovasc. Res.* **118**, 53–64 (2022). doi: 10.1093/cvr/cvab047; pmid: 33620071
63. E. Tzahor, S. Dimmeler, A coalition to heal-the impact of the cardiac microenvironment. *Science* **377**, eabm4443 (2022). doi: 10.1126/science.abm4443; pmid: 36048959
64. Q. Liu *et al.*, Lung regeneration by multipotent stem cells residing at the bronchioalveolar-duct junction. *Nat. Genet.* **51**, 728–738 (2019). doi: 10.1038/s41588-019-0346-6; pmid: 30778223
65. X. Liu *et al.*, Functional ProTracer identifies patterns of cell proliferation in tissues and underlying regulatory mechanisms. *NPJ Regen. Med.* **8**, 41 (2023). doi: 10.1038/s41536-023-00318-y; pmid: 37537178

66. L. Miquerol *et al.*, Architectural and functional asymmetry of the His-Purkinje system of the murine heart. *Cardiovasc. Res.* **63**, 77–86 (2004). doi: 10.1016/j.cardiores.2004.03.007; pmid: 15194464
67. H. Zhao *et al.*, Identifying specific functional roles for senescence across cell types. *Cell* **187**, 7314–7334.e21 (2024). doi: 10.1016/j.cell.2024.09.021; pmid: 39368477
68. J. J. Weyers, D. D. Carlson, C. E. Murry, S. M. Schwartz, W. M. Mahoney Jr., Retrograde perfusion and filling of mouse coronary vasculature as preparation for micro computed tomography imaging. *J. Vis. Exp.* **3740**, e3740 (2012). doi: 10.3791/3740; pmid: 22353785
69. E. Cano *et al.*, Intramyocardial sprouting tip cells specify coronary arterialization. *Circ. Res.* **135**, 671–684 (2024). doi: 10.1161/CIRCRESAHA.124.324868; pmid: 39092506
70. O. M. Leung *et al.*, Regulatory T cells promote apelin-mediated sprouting angiogenesis in type 2 diabetes. *Cell Rep.* **24**, 1610–1626 (2018). doi: 10.1016/j.celrep.2018.07.019; pmid: 30089270
71. Z. Liu, C. K. Ho, Tracing the origins of de novo coronary collateral formation in cardiac repair. Zenodo (2026); https://doi.org/10.5281/zenodo.20603120.

## ACKNOWLEDGMENTS

We thank R. Adams (Max Planck Institute for Molecular Biomedicine) and Q. Chen (Guangzhou Institutes of Biomedicine and Health) for kindly sharing the *Bmx-CreER* line. We thank Shanghai Model Organisms and GemPharmatech for mouse generation and the Animal Core Facility of the CEMCS for mouse husbandry. **Funding:** This work was supported by the National Key Research & Development Program of China (2024YFA1803302 and 2023YFA1800700 to B.Z.); Shenzhen Medical Research Fund (C2504001 to B.Z.); National Science Foundation of China (82688201 to B.Z. and 32500629 to M.Z.); CAS Strategic Priority Research Program of CAS (XDB0990101 to B.Z.); CAS Project for Young Scientists in Basic Research (YSBR-012 to B.Z.); Research Grants Council of Hong Kong (RFS2223-4S04 to K.O.L.); Youth Innovation Promotion Association CAS (B.Z.); Shanghai Pilot Program for Basic Research–CAS, Shanghai Branch (JCYJ-SHFY-2021-006 to B.Z.); Natural Science Foundation of Shanghai-Youth Projects (25ZR1402525 to M.Z.); Shanghai Municipal Science and Technology Major Project (B.Z.); Innovative research team of high-level local universities in Shanghai (B.Z.); CAS-Croucher Funding Scheme for Joint Laboratories (CAS24401 and CAS24CU01 to B.Z. and K.O.L.); and the New Cornerstone Science Foundation through the New Cornerstone Investigator Program (B.Z.). **Author contributions:** M.Z. designed the study, performed the experiments, and analyzed the data. M.H. generated the *Kdr-CreER;Cx40-Dre;Cx40-IR* system. Y.H. and H.Q. performed the hESC-EC experiments, CUT&RUN-seq, and analyzed the data. Z.L. and C.K.H. performed the sequencing-related experiments and analyzed data. Y.W. bred mice and performed genotyping. X.H., Q.-D.W., and X.M. bred mice, performed experiments, analyzed data, or provided intellectual input for this study. K.O.L. and B.Z. conceived and designed the project, interpreted the data, and drafted the manuscript. **Competing interests:** The authors declare that they have no competing interests. The funders had no role in the study's design; the collection, analyses, interpretation of data; the writing of the manuscript; or the decision to publish the results. **Data, code, and materials availability:** All data are available in the main text or supplementary materials. All the newly generated mouse lines used in this study are available from B.Z. under a materials transfer agreement with the Center for Excellence in Molecular Cell Science, Chinese Academy of Sciences. The raw scRNA-seq and RNA-seq data generated in this study are deposited in Genome Sequence Archive (GSA; https://ngdc.cncb.ac.cn/gsa) under accession no. PRJCA063486. The raw CUT&RUN sequencing data generated in this study are deposited in the NCBI Gene Expression Omnibus (GEO) under accession no. GSE334830. The codes used in the scRNA-seq, RNA-seq, and CUT & RUN-seq are available on Zenodo (*71*), with persistent access at https://doi.org/10.5281/zenodo.20603120. 

## SUPPLEMENTARY MATERIALS

science.org/doi/10.1126/science.ady3027
Figs. S1 to S12; Tables S1 to S3; MDAR Reproducibility Checklist
Submitted 17 April 2025; resubmitted 5 May 2026; accepted 12 June 2026
10.1126/science.ady3027

# Tracing the origins of de novo coronary collateral formation in cardiac repair

Mingjun Zhang, Maoying Han, Yangfeng Hou, Zixin Liu, Yilian Wang, Xiuzhen Huang, Cheng Kiu Ho, Hang Qu, Qing-Dong Wang, Xin Ma, Kathy O. Lui, and Bin Zhou

*Science* **393** (6813), eady3027. DOI: 10.1126/science.ady3027

**Editor's summary**

A myocardial infarction occurs when blood flow through one of the coronary arteries is obstructed, causing ischemic damage to the myocardium supplied by this artery. In some cases, though, patients have collateral blood vessels that bypass the obstruction and provide some blood flow to the downstream tissue, decreasing the extent of cardiac damage and risk of death. To determine the origin of these collaterals, Zhang *et al*. engineered a number of mouse models with fluorescent reporters tracing the formation of different types of blood vessels. They determined that coronary collaterals are derived from capillaries, not from other arteries, which may help inform strategies to promote collateral formation. —Yevgeniya Nusinovich







*Science* (ISSN 1095-9203) is published by the American Association for the Advancement of Science. 1200 New York Avenue NW, Washington, DC 20005. The title *Science* is a registered trademark of AAAS.